Arab American University

Faculty of Graduate Studies

Formation and characterization of AlSb/CdS heterojunction

By

Lara Omar Abd Alqader Abu Samen

Supervisor

Prof. Dr. Atef Fayez Qasrawi

This Thesis was submitted in partial fulfillment of the requirements for

the Master's degree in Physics

July/2021

Formation and characterization of AlSb/CdS heterojunctions

By

Lara Omar Abd Alqader Abu Samen

This thesis was defended successfully on July 14th 2021 and approved by:

Committee members Signature

1. Supervisor: Prof. Dr. Atef Fayez Qasrawi

2. External examiner: Assoc. Prof. Dr. Khaled Ilaiwi

3. Internal examiner: Prof. Dr. Hazem Khanfar

Declaration

The work provided in this thesis, unless otherwise referenced, is the researcher's own work and has not been submitted elsewhere for any other degree or qualification.

العمل المقدم في هذه الرسالة، ما لم تتم الاشارة الى خلاف ذلك، هو عمل الباحث الخاص ولم يتم تقديمه في أي مكان آخر للحصول على أي درجة أو مؤهل آخر.

Student's Name: Lara Omar Abd Alqader Abu Samen

Signature: 

Data: 14/12/2021

Acknowledgments

In the name of God, the Most Gracious, the Most Merciful, and my success is only by Allah. My master's thesis has been completed from my prestigious university, Arab American University, thanks to God. I extend my sincere thanks and appreciation to all faculty members. In particular, the honorable Professor Dr. Atef Qasrawi, who has spared no effort in order for this thesis to see the light. God rewarded him with the best reward. And I also thanks to the external examiner, the virtuous Prof. Dr. Khaled Ilaiwi, and the internal examiner, the virtuous Prof. Dr. Hazem Khanfar. All thanks and love to my beautiful family who supported me all the time. My dear parents, (my mother and my father), whose prayers for me was the secret of my success. My hope and happiness are you.

Thank are also due to the kind assistance Rana Daraghmeh who provided me with support and assistance, both in the practical and theoretical side throughout the work. My wonderful friends, Wala, Bayan and Mayamin, who were distinguished by loyalty and giving, and we walked together on the path to success. Praise be to God , and we will continue.

Abstract

Formation and characterization of AlSb/CdS heterojunctions

In this thesis, thin films of Aluminum Antimonide (AlSb) and Cadmium Sulfide (CdS) are prepared by thermal evaporation technique onto glass and Indium Tin Oxide (ITO) substrates under a vacuum pressure of 10^{-4} mbar. The films are structurally, optically and electrically characterized. It was observed that thin films of AlSb and CdS exhibit polycrystalline nature of cubic and hexagonal structures, respectively. The structural parameters including the lattice parameters, the crystallite size, the microstrains, the defect densities and stacking faults are determined. Stacking of CdS onto AlSb, resulted in increased defect density, increased microstrains and decreased crystallite sizes. The structural changes were attributed to the lattice mismatches and the bonding mechanisms. Optically, both of CdS and AlSb/CdS displayed direct optical gap transition with energy band gaps of 2.45 and 2.20 eV, respectively. In spite of it is metallic character, AlSb substrates successfully enhanced the light absorbability (R_λ) in the visible range of light showing a maximum R_λ of 14.8 at 2.21 eV. Analyses of the dielectric spectra have shown that AlSb can exhibit large dielectric constant values in the IR range of light. The dielectric constant of CdS decreased significantly when coated onto AlSb in the IR range. On the other hand, Drude-lorentz modeling of the imaginary part allowed determining the plasmon frequency, drift mobility, oscillator energy and relaxation time at femto second level. While AlSb displayed highest plasmon frequency, CdS showed higher mobility values. Interfacing of both layers resulted in moderate values of drift mobility and plasmon frequency. The values of plasmon frequency being in the gigahertz range nominate the studied films for 4G/5G technologies. Form electrical point of view, the impedance spectroscopy which was

studied in the spectral range of 10-1800 MHz have shown that ITO/AlSb/C (IAC) devices exhibit band pass filter characteristics above 1800 MHz and ITO/AlSb/CdS/C (IACC) show multiband stop filter characteristics above 1200 MHz. Analysis of AC conductivity indicated domination of correlated barrier hoping conduction in IAC devices and combined mechanism of CBH and quantum mechanical tunneling in IACC devices. While the capacitance spectra of IAC samples show decaying trend of variation with increasing frequency, IACC samples displayed three resonance peaks at 217 MHz, 829 MHz and 1098 MHz. To explore the origins of the AlSb formation nature, the structural and electrical characterizations were repeated for the remaining bulky melt of the AlSb source material. One interesting feature is that the tip of the bulk is composed of 43% AlSb and the bottom is composed of 32%. The bulky AlSb displayed band pass filter characteristics above 1600 MHz. The study has shown that the films and bulky samples can be effectively used in optoelectronic applications.

List of Contents

List of Tables

List of Figures

List of Symbols

Symbol	Symbol Meaning
AlSb	Aluminum antimonide
CdS	Cadmium sulfide
ITO	Indium Tin Oxide
IAC	ITO/AlSb/C thin film
IACC	ITO/AlSb/CdS/C thin film
Δ	The lattice mismatch
a_e	Epitaxial Layer Lattice Constant
a_s	Substrate Lattice Constant
Eg	Energy band gap
t_c	Critical Thickness
θ	Bragg angle
d	Inter-planner distance
λ	Wavelength
n	Integer
D	Crystallite Size
β	The peak broadening at full width half maximum peak in radians
k	The shape factor
α	Absorption Coefficient
E_e	The width of the band tails
ε_1 (E)	The real part of the dielectric constant
ε_2 (E)	The imaginary part of the dielectric constant
K (E)	Extinction coefficient
R (E)	The normal incidence reflectivity
$\boldsymbol{\varepsilon}_{eff}$	The effective dielectric constant
μ_{eff}	The effective permeability
ε_s	The permittivity of semiconductor
χ	The electron affinity
CBH	Correlated Barrier Hopping
QMT	Quantum Mechanical Tunneling
w_{pn}	Plasmon frequency of electron
w_{pp}	Plasmon frequency of hole
G	Conductance
σ	Conductivity
τ_o	Relaxation time
ν	Phonon frequency
C	Capacitance
ρ	Reflection coefficient
L_r	Return loss

Chapter One

Introduction

Aluminum antimonide (AlSb) thin films have attracted the attention owing to their wide range of applications. In general, they have applications as Electro-optical devices [1] and as x-ray detectors [2]. In addition, they are used as absorbent layers in thin-films solar cells [3, 4-5]. AlSb thin films capture the interest as a photovoltaic material suitable for solar cell fabrication [4, 6] and other opto-electronic applications [7, 8]. In that sector, the cell conversion efficiency was identified to be 18.07%. Moreover, AlSb films have potential applications in radiation detection [2, 9-10]. In the same context, AlSb as smart materials can be used in the design of temperature based photo sensing device [9, 11]. Heterojunctions that employ AlSb as interfacing layers are beneficial for thermoelectric applications [12, 13]. Films of AlSb having a high electron mobility can be used in applications which require high speed electronic devices [10]. As another AlSb heterojunction devices they are used to produce thin film transistors with a band gap of 1.62 eV [4, 9, 14].

On the other hand, Cadmium Sulfide (CdS) as a semiconductor of the II-VI group is known to exhibit a wide band gap of 2.4 eV [15, 16]. They are used in many applications as microwave receivers [17]. They exhibit a negative capacitance effect and form band stop filters. As another type of application, CdS is attractive as photoelectrochemical cell (PEC) for bioanalysis applications [18, 19]. Carbon decorated nanostructured CdS fiber networks show stable photocurrent. CdS is also used as photo catalytic material [15, 20-22]. The performance of CdS-nanowires as photoelectrochemical solar cells and sensitized solar cells is remarkable [23-26]. In other work, CdS also has applications as photoconductors [27] and as quantum dots.

Fluorescence sensors of this material show enhanced sensing features [28]. These quantum dots are also regarded as supercapacitors [29]. Furthermore, optical-nonlinear-limiting applications were noticed when CdS films were doped with Tin [30].

Literature data included information about preparation using thermal evaporation technique for preparing p-type AlSb thin-film. The films were prepared on n-type Si substrates [3]. It is reported that these films are of the best properties and good quality. In another work, magnetron sputtering technology is used for preparation of Cu doped AlSb [31]. The produced films are annealed at 500 °C and found to reduce deliquescence speed. Several researchers have used the pulsed laser deposition (PLD) method [4]. These studies show a reduced band gap of 1.4 eV of the AlSb-Zn film. In addition, AlSb thin films are prepared by a screen printing and sintering method [7, 32]. The DC conductivity measurements affirmed that these films have a semiconducting nature [7, 14, 33]. As another technique, single step electrodeposition was used to grow AlSb films on the brass sheet. The X-ray diffraction shows that the films have a polycrystalline nature. The SEM studies indicated that the AlSb films exhibit uniform, large and smooth spherical grains morphology. The energy dispersive X-ray spectroscopy (EDAX) studies show that the electrodeposited AlSb thin films are nearly stoichiometric [33].

Many techniques have been employed to improve the physical properties of CdS. For example, evaporation a layer of yttrium between two layers of CdS using physical vapor deposition. This technique enhanced the light absorbability by ~5 times near ~1.74 eV [17]. In addition, the praseodymium doping to Cadmium Sulfide was also able to improve the optoelectrical properties of CdS thin films [34]. These films were

fabricated by using spray pyrolysis technique. The energy gap was found to lie in the range of 2.40–2.44 eV.

In the light of the mentioned information about AlSb and CdS thin films, we were motivated to construct a heterojunction device from both materials and test its possible applications. Here in this work, AlSb thin films of thickness of 130 nm are used as a substrate to prepare semiconductor layers of CdS by the thermal evaporation method under high vacuum pressure. The produced films are investigated by means of X-ray diffraction, optical spectrophotometry and impedance spectroscopy techniques.

Chapter Two
Theoretical Background

2.1 Heterojunction

The heterojunction is the junction that forms between two dissimilar semiconducting materials with unequal band gaps. The difference in the band gaps of these two semiconductors provides very exciting phenomena for semiconductor-device applications. The heterojunction devices are prepared by different techniques, including molecular epitaxial technique, thermal evaporation technique, flash evaporation technique. Two materials with similar lattice constants but different energy gaps can make a good combination for heterojunction devices [35].

2.1.1 Lattice mismatch

The lattice mismatch (Δ) is defined as:

$$\Delta = \frac{|a_e - a_s|}{a_e} \tag{2.1}$$

Where a_e and a_s, are the lattice parameters of the epitaxial and substrate layers, respectively [35]. A severe lattice mismatch can cause dislocations at the interface. Which results in electrical defects such as interface traps. It became clear that good-quality heteroepitaxy can continue to grow if the lattice parameters are not significantly mismatched, provided the epitaxial-layer thickness is small enough. The amount of lattice mismatch is directly related to the maximum allowed epitaxial layers. While, for a thick heteroepitaxial layer, dislocations at the interface are unavoidable because the physical mismatched terminating bonds at the interface. Dislocations can be avoided in a thin enough layer by physically straining until its lattice constant becomes the same as the substrate layer [35]. Fig. 2.1 shows how the

epitaxial lattice parameter a_e is strained to follow that of the substrate a_s (the epitaxial layer follows the lattice of the substrate).

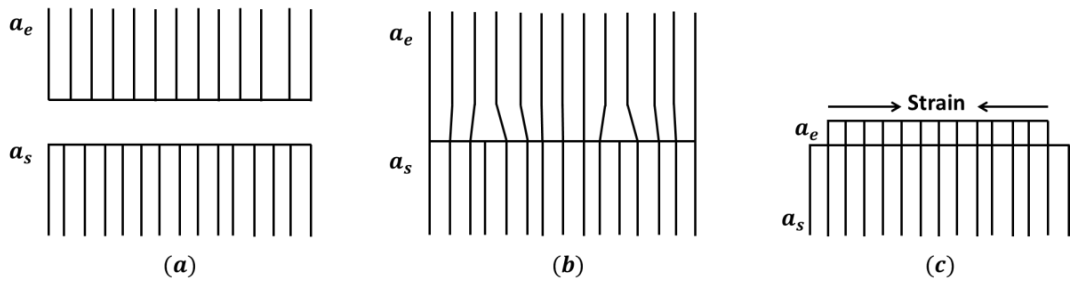

Figure 2.1: Two materials with partially mismatched lattice parameters a_e and a_s. (a) the materials are isolated from each other. (b) with a thick heteroepitaxy layer, the epitaxial layer stretched having dislocations at the interface. (c) with a thin heteroepitaxy layer, the epitaxial layer strained without dislocations at the interface.

2.1.2 Critical thickness

During epitaxial layer growth, the first few layers are coherent with the matrix, and the film lattice could suffer tetragonal distortion. As the thickness of the film increases, dislocations tend to nucleate, and this partially relaxes the strain caused by lattice mismatch, and the thickness at which this occurs is defined as the critical thickness (t_c). The good quality of heterojunctions requires that the epitaxial-layer thickness to be small enough.

The critical thickness (t_c) of the strained layer is given by equation, [35]

$$t_c = \frac{a_e}{2\Delta} \tag{2.2}$$

By substituting equation (2.1), the equation of critical thickness becomes:

$$t_c = \frac{{a_e}^2}{2|a_e - a_s|} \tag{2.3}$$

2.2 The X-ray diffraction (XRD)

X-ray diffraction is an effective technique to detect information about the structure of solid-state materials. As shown in Fig. 2.2, basically, the XRD device consists of the

X-ray source, a sample stage and the X-ray detector. In this figure, the angle θ is located between the plane of the sample and the X-ray source. Also, the angle 2θ is placed between the X-ray source and the detector. The incident beam of monochromatic X-ray is scattered by each atom inside the sample.

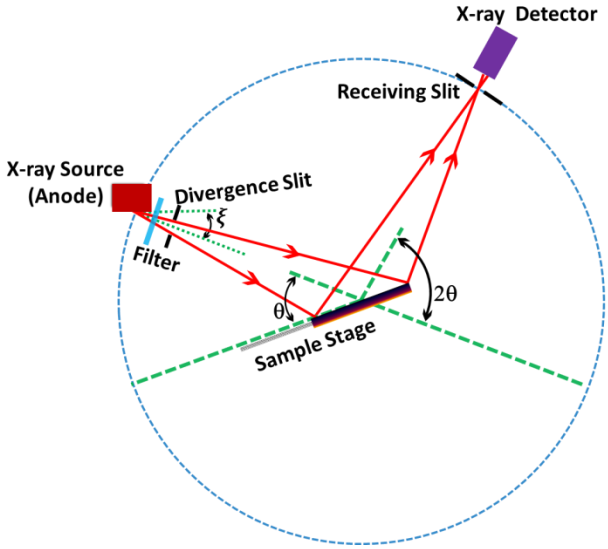

Figure 2.2. The schematic diagram of the X-ray diffractometer [36].

If the scattered beams are in phase, then constructive interference occurs and the crystalline nature of materials appears, otherwise the destructive interference occurs and the amorphous nature of materials appears. In addition, the maximum intensity will occur at the specific angle in a particular plane orientation. The angle values (2θ) of the peak significantly depend on the wavelength of the anode material of the X-ray tube. Copper X-ray tubes with a wavelength of 1.5418 Å were used for XRD production. Copper K-alpha is the X-ray energy that is often used in lab scale X-ray devices. The energy of Cu-Kα is about 8.04 KeV. The XRD patterns can be clearly observed. The interplanar distance between two planes of material atoms is easy to determine with the help of Bragg's law. After calculating the interplanar distance, the lattice parameters, the lattice constant and also the crystalline structure of the material can be determined.

2.2.1 Bragg's law

X-ray diffraction analysis is based on Bragg's law. It indicates that all of the rays scattered from atoms at same locations on parallel planes, as seen in Fig. 2.3, which leads to an amplified signal. Bragg's law relates the inter-planar distance between the atomic planes (d), the angle diffraction (θ) and the wavelength of the reflected X-ray as follows [37]:

$$2d \sin\theta = n\lambda \tag{2.4}$$

Where d is the inter-planer distance between two atomic planes which is measured in angstrom, θ is the angle between the incident beam and the plan surface, n is a positive integer representing the diffraction order and λ is the X-ray wavelength which is equals to 1.5405 Å for Copper X-ray tube along the $K\alpha$ line.

The condition of constructive interference occurs when the path difference between the two waves is equal to multiple integers of the wavelength as Bragg's law shows.

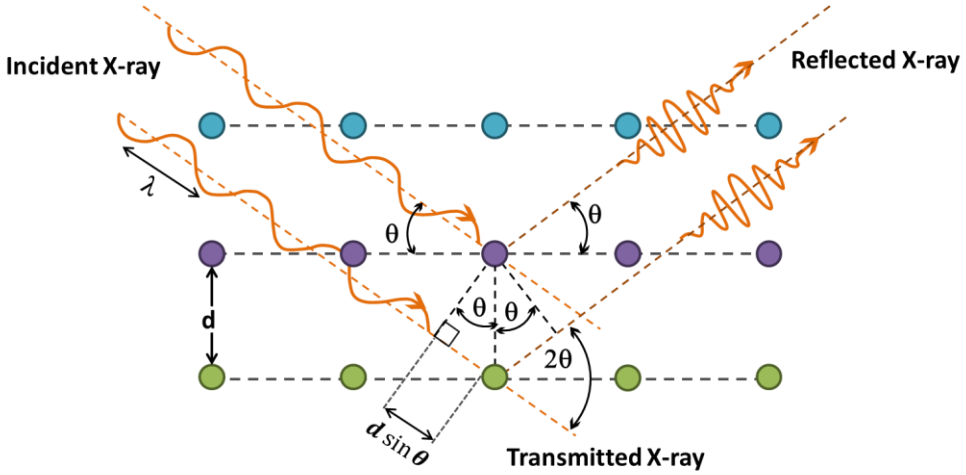

Figure 2.3: The schematic diagram of Bragg scattering on the lattice surface.

2.2.2 Scherrer Equation

Scherrer equation is a simple and well-known expression for calculating the crystallite size (D) from the X-ray diffraction peaks [38]. The Scherrer equation can be obtained in a simple method by taking the derivative of Bragg's law, multiplying both sides of

Bragg's equation (2.4) by an integer m, and replacing md by t, where t is the crystal thickness and assumes $n = 1$.

$$m\lambda = 2\,md\sin\theta \tag{2.5}$$

$$m\lambda = 2\,t\sin\theta \tag{2.6}$$

Equation (2.6) represents the m^{th} order reflection from a set of planes with an inter-planar distance t.

Derive both sides of the equation (2.6):

$$0 = 2\Delta t\sin\theta + 2t\cos\theta\,\Delta\theta \tag{2.7}$$

$$t = \frac{\Delta t\,.\sin(\theta)}{\cos(\theta)\ \Delta\theta} \tag{2.8}$$

Since $\Delta\theta$ maybe positive or negative, the absolute value must be used.

Using $\Delta t = d, t = D$, and substituting $(\frac{\lambda}{2})$ for $d\sin\theta$ from Bragg's law, to get:

$$D = \frac{\lambda}{2\cos(\theta).\Delta\theta} \tag{2.9}$$

$\Delta\theta$ refers to the half width of the peak, so $2\Delta\theta$ is the full width of the peak at half maximum (β). Substituting β for $2.\Delta\theta$, where is the angular width, (D) is the crystallite size equation:

$$D = \frac{\lambda}{\beta\cos\theta} \tag{2.10}$$

Finally, many complicated derivations indicated that the exact Sherrer's formula, where λ is multiplied by a factor of k.

$$D = \frac{k\lambda}{\beta\cos\theta} \tag{2.11}$$

Where k is the Scherrer constant, which depends on the crystalline shape, Bragg and Miller indices show that the value of k is about 0.94 [39], λ is the wavelength of the incident X-ray beam, β is the line broadening at half the maximum intensity measured

in radians, and θ is the Bragg angle. Fig. 2.4 illustrated the full half maximum intensity.

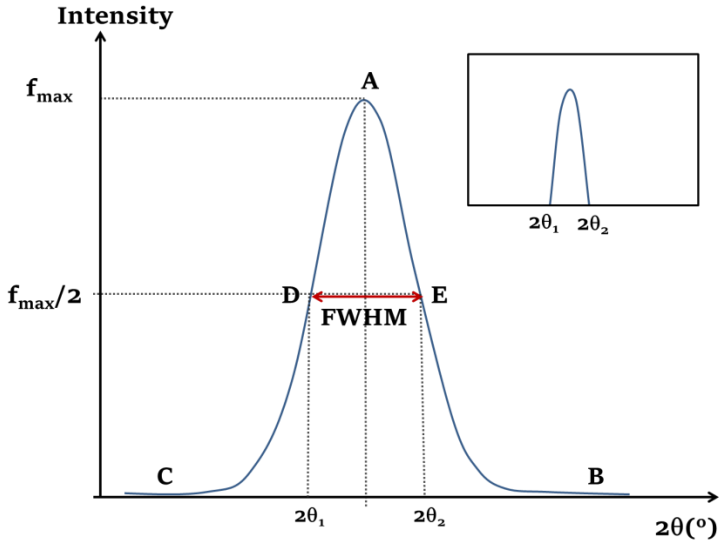

Figure 2.4: The full width at half maximum (FWHM)

The full width at half maximum can be calculated as can be seen from Fig. 2.4:

$$D = \frac{B + C}{2} \tag{2.12}$$

$$E = \frac{A - D}{2} \tag{2.13}$$

The position value of the full width high maximum (FWHM) $= E + D$

Then β can be obtained from the following equation:

$$\beta = (|2\theta_2 - 2\theta_1|) \times \left(\frac{3.14}{180}\right) \tag{2.14}$$

2.2.3 Structural Parameters

Different structural parameters were measured by using the XRD pattern study. Some of these parameters are the grain size(D), lattice strain (ε), dislocation density (δ) and stacking faults ($SF\%$). These parameters are determined from the broadening width β ($FWHM$) (2.14) of the most intensive peak upon the following relations [40].

The grain size (D) is the diameter of an individual grain in the crystal [41]. It is calculated using the Scherrer formula:

$$D = \frac{0.94\,\lambda}{\beta \cos\theta} \tag{2.15}$$

The lattice strain (ε) is the ratio of contraction or expansion in bond lengths to the original bond lengths [41]. It is measured by the following equation:

$$\varepsilon = \frac{\beta}{4\tan(\theta)} \tag{2.16}$$

The dislocation density (δ) is a measure of the number of dislocations in a unit volume of the crystal, and it can be calculated by the following equation:

$$\delta = \frac{15\,\varepsilon}{a\,D}\ \ lines/cm^2 \tag{2.17}$$

Where ε is the strain, a is the lattice constant in a-axis and D is the grain size.

Fig. 2.5 displays the two types of strain and its effect on the crystal structure, also it shows the behavior of the peak if the strain occurred.

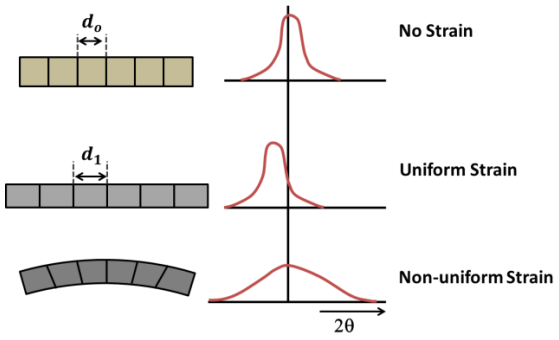

Figure 2.5: The effect of strain on the crystal atoms.

The stacking fault ($SF\%$) is a type of defect that characterizes the crystallographic plane disordering. It is classified as a planar defect that can occur in crystalline material [41].

$$SF\% = \frac{2\,\pi^2\beta}{45\sqrt{3\tan(\theta)}} \times 100\% \tag{2.18}$$

2.2.4 Crystallography

A crystal consists of a periodic pattern of unit cells arranged into a lattice. The unit cell could contain a single atom or multiple atoms arranged in a fixed pattern. Crystalline solid materials consist of planes of atoms separated by a distance d. It can be planned into many atomic planes, each with a different d spacing, a, b and c lengths, and α, β and γ angles between a, b and c are lattice constants which can be measured by XRD. Atoms can be arranged in crystals in fourteen different three-dimensional configurations known as Braves lattice. These Braves lattice are classified into seven systems (structures), as seen in Table 2.1 below.

Table 2.1. The $3D$ Braves lattice for solid state materials and their conditions [37].

Crystal structure	Conditions	Number of Braves lattice
Cubic	$a_1=a_2=a_3$ $\alpha=\beta=\gamma=90^0$	3
Hexagonal	$a_1=a_2\neq a_3$ $\alpha=\beta=90^0$, $\gamma=120^o$	1
Trigonal	$a_1=a_2=a_3$ $\alpha=\beta=\gamma<120^o\neq90^0$	1
Tetragonal	$a_1=a_2\neq a_3$ $\alpha=\beta=\gamma=90^0$	2
Orthorhombic	$a_1\neq a_2\neq a_3$ $\alpha=\beta=\gamma=90^0$	4
Monoclinic	$a_1\neq a_2\neq a_3$ $\alpha=\beta=90^0\neq\gamma$	2
Triclinic	$a_1\neq a_2\neq a_3$ $\alpha\neq\beta\neq\gamma\neq90^0$	1

Each group of Braves lattice is divided into several types based on structural characteristics, for a total of 14 Braves lattice. The orientation of a crystal plane or a surface can be described by considering how the plane (or any parallel plane) intersects the solid's main crystallographic axis. The Miller indices (hkl) are assigned according to a set of rules. These are a set of numbers that quantify the intercepts and can thus be used to uniquely characterize the plane of surfaces.

2.2.5 Derivation of the spacing interplanar of cubic lattice:

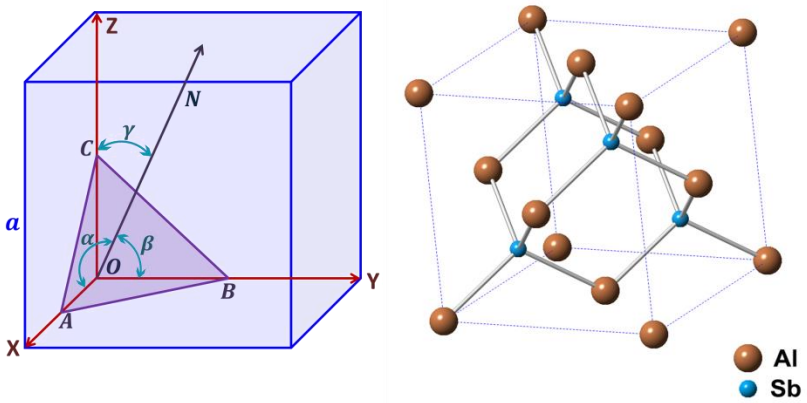

Figure 2.6: The cubic lattice structure.

The inter planner spacing d_{hkl} is the perpendicular distance between parallel planes.

The intercepts of the main plan on the three a'es:

$$OA = a/h$$

$$OB = a/k$$

$$OC = a/l$$

From the figure: (Interplanar spacing d_{hkl} is equal to the origin along the normal (N) direction of the plane)

$$cos\,\alpha = N/\,OA\; = dh/a$$

$$cos\,\beta = \;N/\,OB\; = dk/a$$

$$cos\,\gamma = \;N/\,OC\; = dl/a$$

Using the relationship of directional cosines:

$$cos^2\,\alpha + \;cos^2\beta + \;cos^2\,\gamma = 1$$

We obtains

$$d_{cubic\ lattice\ hkl} = \frac{a}{\sqrt{h^2 + k^2 + l^2}} \qquad (2.19)$$

2.2.6 Derivation of the spacing interplanar of hexagonal lattice:

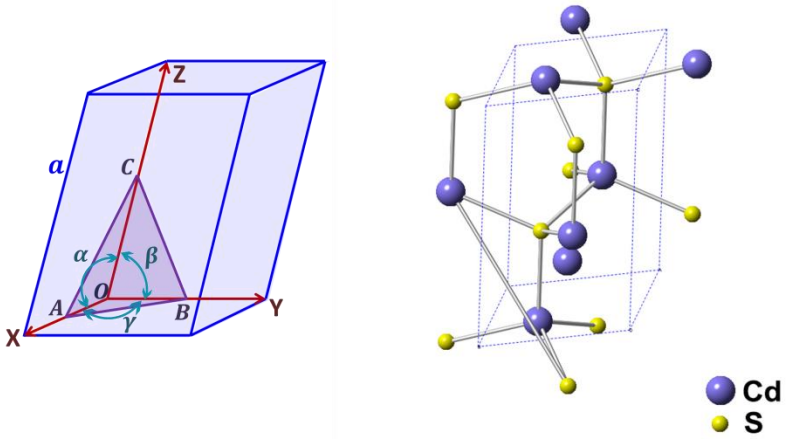

Figure 2.7: The hexagonal lattice structure.

A hexagonal structure where the angle between basic vectors a and b is 120°

For the hexagonal structure we have:

$$a = b \neq c$$

$$\alpha = \beta = 90^o$$

$$\gamma = 120^o$$

By using the triclinic equation [42] to define the interplaner spacing:

$$\frac{1}{d_{hkl}^2} = \frac{1}{[1 + 2\cos(\alpha)\cos(\beta)\cos(\gamma) - \cos^2(\alpha) - \cos^2(\beta) - \cos^2(\gamma)]} \times \left[\frac{h^2 \sin^2(\alpha)}{a^2} + \frac{k^2 \sin^2(\beta)}{b^2} + \frac{l^2 \sin^2(\gamma)}{c^2} + \frac{2hk}{ab}(\cos(\alpha)\cos(\beta) - \cos(\gamma)) + \frac{2kl}{bc}(\cos(\beta)\cos(\gamma) - \cos(\alpha)) + \frac{2lh}{ca}(\cos(\gamma)\cos(\alpha) - \cos(\beta))\right]$$

Substitute the condition of the hexagonal structure to get:

$$\frac{1}{d_{hkl}^2} = \frac{1}{[1 + \cos^2(120)]} \times \left[\frac{h^2 + k^2}{a^2} + \frac{l^2 \sin^2(120)}{c^2} + \frac{2hk}{a^2}(-\cos(120))\right]$$

$$\frac{1}{d_{hkl}^2} = \frac{1}{\left[1+\frac{1}{4}\right]} \times \left[\frac{h^2+k^2}{a^2} + \frac{l^2 \times \frac{3}{4}}{c^2} + \frac{2hk}{a^2}\left(\frac{1}{2}\right)\right]$$

As a result, we get:

$$\frac{1}{d_{hkl}^2} = \frac{4}{3}\left(\frac{h^2+hk+k^2}{a^2}\right) + \frac{l^2}{c^2} \tag{2.20}$$

2.3 Optical properties

Suppose a medium (semiconductor material) is exposed to a light beam of a specific propagation thickness. Then the incident beam may be transmitted or reflected outside the medium or propagated through the medium. Linear optical propagation involves four processes: refraction, absorption, luminescence and scattering. Fig. 2.8 displayed the transmittance, reflectance and the absorbance of incident light on the optical medium.

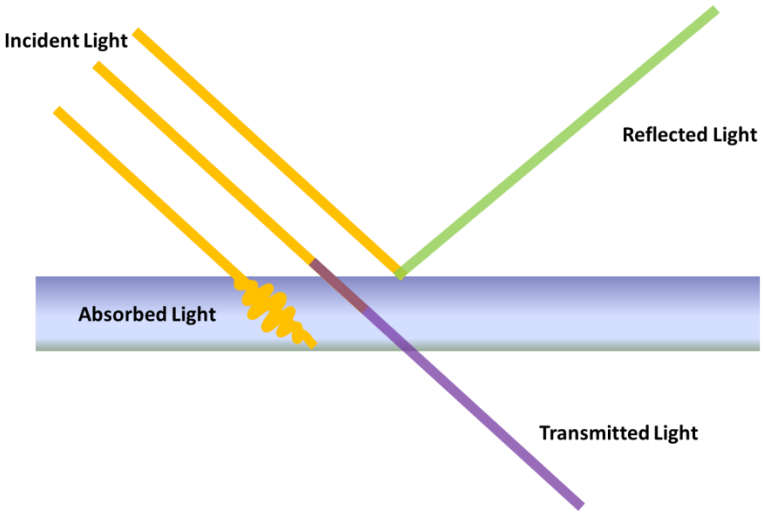

Figure 2.8. The transmittance, reflectance and absorbance of a light incident on the optical material.

Refraction can be referred as light bending when it passes from one interface to another. Light bending at the interface between two mediums is described by snell's law [35].

$$n_1 \sin\theta_1 = n_2 \sin\theta_2 \tag{2.21}$$

Absorption is essentially related to the propagation of light frequency. When the light frequency is equal to the frequency of solid material oscillation, then the light will be absorbed.

The study of optical properties includes the measurement of transmittance (T), reflectance (R), absorption coefficient (α), energy band gap (Eg), refractive index and dielectric constant (ε).

2.3.1 The absorption coefficient (α)

If the photon is absorbed inside the material, it will be able to excite an electron and transferred from the valence band to the conduction band. The absorption of light by an optical medium is measured by its absorption coefficient $\alpha(h\nu)$. Which determines how far into a material light of a specific wavelength can penetrate before being absorbed.

Consider a light beam propagating in the z direction, and if the light intensity at point z is $I(z)$, the decrease in light intensity in an incremental slice thickness (dz) is given by:

$$dI = -\alpha\, I(z)dz \tag{2.22}$$

Integrate both sides of the equation (2.22), to obtain a formula of Beer's law [43] which states:

$$I(z) = I_o\, e^{-\alpha z} \tag{2.23}$$

Where I_o is the light intensity at $z = 0$, α is the absorption coefficient, and z is the material thickness. Since the absorption coefficient is a strong function that depends on frequency, then the optical material can absorb one color without the other [44]. Transmissivity (T) is the efficiency at which the radiant energy is transmitted through

a volume. The light transmissivity in an optical medium of thickness l can be written as [44]:

$$T = (1 - R_1)(1 - R_2)\, e^{-\alpha l} \tag{2.24}$$

Where R_1 and R_2 are the reflectivities of the front and back surfaces, respectively. Thus, the terms $(1 - R_1)$ and $(1 - R_2)$ reflect the transmission of the front and back layer surfaces of the medium, respectively. The expression $(e^{-\alpha l})$ represents an exponential relation decrease in the light intensity in accordance with Beer's law.

Assume that R_1 and R_2 are equal, then the equation (2.24) becomes:

$$T = (1 - \mathrm{R})^2\, e^{-\alpha l} \tag{2.25}$$

As two materials are deposited on the glass substrate, the transmissivity becomes:

$$T = (1 - R_1)(1 - R_2)(1 - R_3)e^{-\alpha l} \tag{2.26}$$

The absorbance (A) of a grown film can be calculated if the transmittance (T) and reflectance (R) of the film are known:

$$A = -\ln\left(\frac{T}{(1 - R_{glass})(1 - R_{sample})}\right) \tag{2.27}$$

If the thickness of the film (d) is monitored, the absorption coefficient $\alpha(h\nu)$ can be connected to the absorbance (A) of the film using the following relation:

$$A = \alpha\, d \tag{2.28}$$

Thus, the absorption coefficient $\alpha(h\nu)$ at thickness $l = d$ is written as:

$$\alpha(h\nu) = -\frac{1}{d}\ln\left(\frac{T}{(1 - R_1)(1 - R_2)(1 - R_3)}\right) \tag{2.29}$$

Similarly, the absorption coefficient for four materials deposited in a glass substrate is given by:

$$\alpha = -\frac{1}{d}\ln\left(\frac{T}{(1 - R_1)(1 - R_2)(1 - R_3)(1 - R_4)}\right) \tag{2.30}$$

In this work R_1, R_2, R_3 and R_4 represent the reflectance of glass, AlSb, CdS and AlSb/CdS, respectively, and d is the layer thickness of the thin film.

2.3.2 Tauc's equation and band gap measuring:

Tauc's equation is used in accordance with absorption coefficient spectra to calculate the optical band gap of semiconductors and heterojunctions. Tauc's equation indicates that the energy band gap is directly proportional to $(\alpha E)^p$. Where the exponent (p) implies the nature (characteristic) of the transition. The Tauc's equation formula is given in the equation (2.31) below [45].

$$(\alpha E)^p = B\left(E - E_g\right) \qquad (2.31)$$

Where B is a constant that depends on the electron transition probability, E is the incident photon (light) energy, E_g is the energy band gap and p is an index that describes the optical absorption process.

The parameter p theoretically equal to $2, \frac{1}{2}, 3\ or\ \frac{3}{2}$ corresponding to indirect allowed, direct allowed, indirect forbidden and direct forbidden electron transitions between valence and conduction band, respectively.

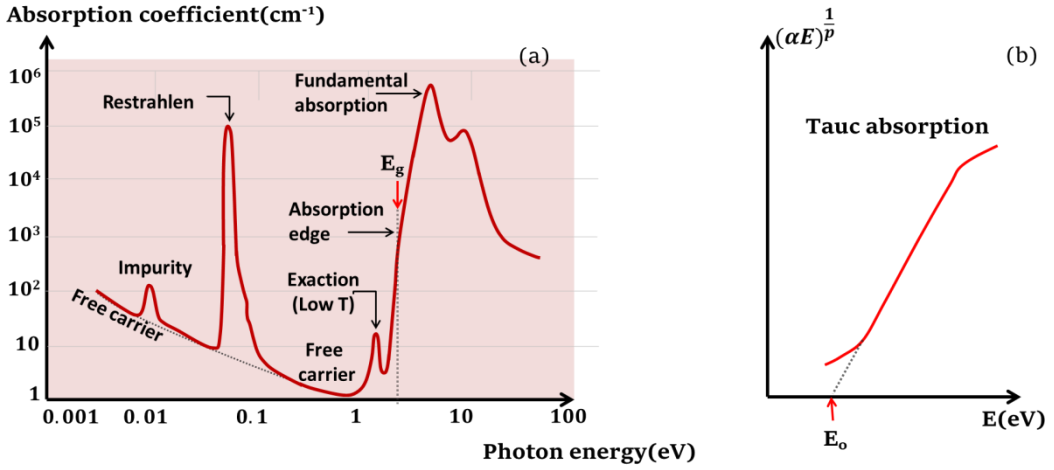

Figure 2.9: (a) Absorption coefficient plotted as a function of the photon energy in a typical semiconductor and (b) Taue absorption spectra.

Generally, the Tauc relation is:

$$\alpha\hbar\omega \propto \left(\hbar\omega - E_g\right)^p \tag{2.32}$$

Where $\hbar\omega$ represent the incident photon energy, from $(\alpha E)^{1/p} - E$ plot and by taking the widest range of linear data in the high absorption region upon linear fitting, the energy gap for semiconductor materials can be determined from the intercept of the photon energy axis $(E - axis)$. Fig. 2.9 shows the absorption coefficient spectra plotting versus the photon energy (E) and the energy gap (E_g) determination, which requires $(\alpha E)^{1/p}$ plotting versus the photon energy (E).

2.3.3 Direct and indirect transition:

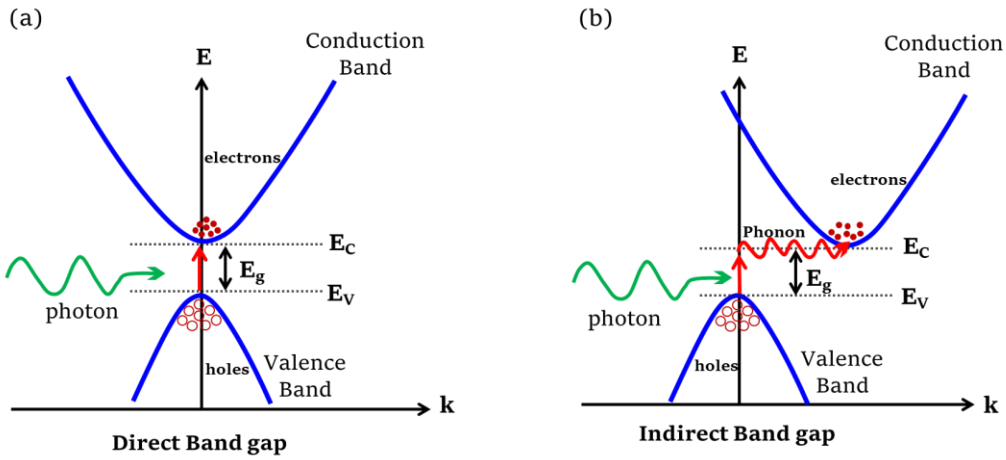

Figure 2.10: Incident photons cause solid interband (a) direct and (b) indirect transitions.

The band gap energy is the energy range between the valence band and conduction band where the electron states are forbidden inside it. Fig. 2.10 illustrates the direct and indirect band gap semiconductors. In the direct band gap, the top of the valence band and the bottom of the conduction band appear at the same momentum value. In contrast, the indirect band gap is characterized by the maximum of the valence band and the minimum of the conduction band are dissimilar in momentum value (k-vectors). This difference in k-vectors exhibits misaligned bands that require a phonon

assistance for excited electron to be absorbed into the conduction band. While, for the direct band gap materials, a change in the crystal momentum (k) is not involved and no phonon assistance is needed.

2.3.4 Band Tails

Along the absorption coefficient curve and near the optical band edge there is an exponential part dependence on the photon energy called Ubrach tail (band tail) [46]. These tails arise in the disordered, amorphous and low crystalline materials, because these materials have localized electronic states that are extended in the band gap (near the bottom of the conduction band or the top of the valence band).

The Urbach's rule is described as follows:

$$\alpha = \alpha_o \, e^{E/E_e} \tag{2.33}$$

Where α is the absorption coefficient, α_o is a constant, E is the photon energy and E_e is the width of the band tail of the localized state associated with the amorphous state.

Taking the logarithm of the two sides of the equation (2.33), we can obtain a straight line equation. It is given by:

$$\ln \alpha = \ln \alpha_o + \left(\frac{E}{E_e}\right) \tag{2.34}$$

Plotting $ln(\alpha)$ as a function of incident photon energy (E), the enter band energies can be determined from the slope of the straight line.

2.3.5 The refractive index and the dielectric spectra:

The refractive index of a material is a dimensionless number that represents how fast light passes through the material. Which is determined by the incident optical beam's wavelength. A complex refractive index can be used to characterize the light

propagation in optical materials [47]. While the real part accounts for refraction, the imaginary part handles the attenuation. The complex refractive index formula is introduced by the dispersion equation, which is given by the following relations:

$$\widetilde{N}_{complex} = n(\lambda) + ik(\lambda) \tag{2.35}$$

$$= (\varepsilon_r + i\,\varepsilon_{im})^{\frac{1}{2}} \tag{2.36}$$

Where n is the refractive index, k is the extinction coefficient , ε_r and ε_{im} is the real and imaginary dielectric constants, respectively.

The dielectric constant (ε) or relative permittivity is the ratio of material permittivity relative to the vacuum permittivity. The dielectric constant, as the refractive index, is a complex number that consists of real and imaginary parts. To obtain the dielectric constant and derive the relation between the extinction and absorption coefficients, suppose an incident electromagnetic wave propagating in $z - axis$ within a dielectric material compromises an electric field in the x-direction:

$$\vec{E}_x = E_o e^{i(kz-\omega t)} \tag{2.37}$$

Where E_o is the amplitude at $z = 0$, k is a wave vector and ω is the angular frequency. The following equation expresses the relation between k and ω.

$$k = \frac{2\pi}{(\frac{\lambda}{n})} = \frac{n\omega}{c} \tag{2.38}$$

It can be generalized by using the complex refractive index.

$$k = \frac{\omega}{c}\,\widetilde{N}_{complex} \tag{2.39}$$

The electric field, including the incident and reflected waves, becomes:

$$\vec{E}_x = E_o e^{i(\frac{\omega z}{c}\widetilde{N}_{complex}-\omega t)} \tag{2.40}$$

The electric field includes the incident and reflected waves moving along + $z - axis$ and -$z - axis$, respectively:

$$\vec{E}_x = E_1 e^{i(\frac{\omega z}{c} - \omega t)} + E_2 e^{-i(\frac{\omega z}{c} + \omega t)} \quad (2.41)$$

$$E_o = E_1 + E_2 \quad (2.42)$$

Where $E_o, E_1 and\ E_2$ are relating by the continuity equation for H_y tangential magnetic field component at the dielectric surface.

Using Maxwell's equations:

$$\nabla \times \vec{E} = -\frac{\mu}{c}\frac{\partial \vec{H}}{\partial t} = \frac{i\omega\mu}{c}\frac{\partial \vec{H}}{\partial t} \quad (2.43)$$

By applying the curl relative to $z - axis$ to the $x - component$ of the incident electric field, we attain

$$\frac{\partial \vec{E}_x}{\partial z} = \frac{i\omega\mu}{c}\frac{\partial \vec{H}_y}{\partial t} \quad (2.44)$$

The derivative of the equation (2.41) relative to z is:

$$E_o k = E_1 \frac{\omega}{c} - E_2 \frac{\omega}{c} \ = E_0 \frac{\omega}{c} \widetilde{N}_{complex} \quad (2.45)$$

Simplification of the equations (2.45) yields:

$$E_1 + E_2 \quad = E_0 \widetilde{N}_{complex} \quad (2.46)$$

By solving the equations (2.42) and (2.46) we get:

$$\begin{cases} E_2 = \frac{1}{2} E_o \left(1 - \widetilde{N}_{complex}\right) & (2.47) \\ E_1 = \frac{1}{2} E_o \left(1 + \widetilde{N}_{complex}\right) & (2.48) \end{cases}$$

The normal reflectance of the incident is given by the relation:

$$R = \left|\frac{E_2}{E_1}\right|^2 \quad (2.49)$$

Simplifying equation (2.49) by substituting the equations (2.47) and (2.48):

$$R = \left|\frac{1 - \widetilde{N}_{complex}}{1 + \widetilde{N}_{complex}}\right|^2 \quad (2.50)$$

Substitute equation (2.35) in (2.50), to get:

$$R = \frac{1 + n^2 - 2n + k^2}{1 + n^2 + 2n + k^2} \tag{2.51}$$

The unity terms will be ignored in the case of a highly absorbed medium with a significant value of $n\ and\ k$ ($n = k \gg 1$), and equation (2.51) becomes:

$$R = \frac{n^2 - 2n + k^2}{n^2 + 2n + k^2} \tag{2.52}$$

From that,

$$Rn^2 + 2Rn + Rk^2 = n^2 - 2n + k^2 \tag{2.53}$$

$$(R-1)n^2 + 2(R+1)n + (R-1)k^2 = 0 \tag{2.54}$$

Using the solution of square root equation $\left(x = \frac{-b \mp \sqrt{b^2-4ac}}{2a}\right)$to obtain:

$$n = \frac{-2(R+1) \mp \sqrt{4(R+1)^2 - 4(R-1)(R-1)k^2}}{2(R-1)} \tag{2.55}$$

And it can be simplified to:

$$n = -\frac{(R+1)}{(R-1)} \mp \sqrt{\left(\frac{R+1}{R-1}\right)^2 - k^2} \tag{2.56}$$

Thus, the roots are:

$$\begin{cases} n_1 = -\dfrac{(R+1)}{(R-1)} + \sqrt{\left(\dfrac{R+1}{R-1}\right)^2 - k^2} & (2.57) \\ n_2 = -\dfrac{(R+1)}{(R-1)} - \sqrt{\left(\dfrac{R+1}{R-1}\right)^2 - k^2} & (2.58) \end{cases}$$

It is known that the effective dielectric constant (ε_{eff}) is expressed in terms of the dielectric refractive index (n) through the relation:

$$n = \sqrt{\varepsilon_{eff}} \tag{2.59}$$

Thus, the equation (2.56) becomes:

$$\sqrt{\varepsilon_{eff}} = -\frac{(R+1)}{(R-1)} \mp \sqrt{\left(\frac{R+1}{R-1}\right)^2 - k^2} \tag{2.60}$$

Thus, the two distinct solutions of ε_{eff}:

$$\begin{cases} \varepsilon_{eff_1} = -\dfrac{(R+1)}{(R-1)} + \sqrt{\left(\dfrac{R+1}{R-1}\right)^2 - k^2} & (2.61) \\ \varepsilon_{eff_2} = -\dfrac{(R+1)}{(R-1)} - \sqrt{\left(\dfrac{R+1}{R-1}\right)^2 - k^2} & (2.62) \end{cases}$$

To drive the formula of dielectric constant (ε) in the terms of the complex refractive index ($\widetilde{N}_{complex}$):

$$\widetilde{N}_{complex} = \sqrt{\mu\varepsilon} \tag{2.63}$$

Thus, for non-magnetic materials ($\mu = 1$):

$$\widetilde{N}_{complex} = \sqrt{\varepsilon_{eff}} \tag{2.64}$$

Since the dielectric constant is a complex number, it can be written as follows:

$$\varepsilon_{eff} = \varepsilon_r + i\varepsilon_{img} \tag{2.65}$$

Where $\varepsilon_r \; and \; \varepsilon_{img}$ are the real and imaginary parts of the dielectric constant, respectively.

Substituting equation (2.35) for equation (2.64) yields:

$$\left(\widetilde{N}_{complex}\right)^2 = \varepsilon_{eff} = (n + ik)^2 \tag{2.66}$$

$$\varepsilon_{eff} = n^2 - k^2 + i2nk \tag{2.67}$$

Comparing the equations (2.67) and (2.65) to get:

$$\varepsilon_r = n^2 - k^2 \tag{2.68}$$

$$\varepsilon_{img} = 2nk \tag{2.69}$$

Consider that an electromagnetic wave propagates in the $z - direction$ of a medium with the following electric field, to obtain the relation between k and α:

$$\vec{E}(z,t) = E_o e^{i(kz-\omega t)} \tag{2.70}$$

Where E_o is the amplitude at $z = 0\ and\ t = 0$, k is the wave vector and ω is the angular frequency.

The relation between the extinction coefficient $K\ and\ \lambda$ is given by:

$$K = \frac{2\pi}{(\lambda/\widetilde{N})} \tag{2.71}$$

Combining equations (2.35), (2.39), (2.70) and (2.71), thus:

$$K = \frac{\omega}{c}\,(n + ik) \tag{2.72}$$

$$\vec{E}(z,t) = E_o e^{i\left(\frac{\omega n z}{c}-\omega t\right)} e^{-\frac{kz\omega}{c}} \tag{2.73}$$

The optical intensity of a light wave is known to be proportional to the square of the electric field where $I \propto EE^*$, consequently:

$$I \propto\ e^{-\left(\frac{\omega k z}{c}\right)} \tag{2.74}$$

As the upper equation (2.74) is compared to Beer's law (2.23), we reveal that:

$$2\frac{k\omega}{c} = \alpha = \frac{4\pi K}{\lambda} \tag{2.75}$$

Then, relation between K and λ

$$K = \frac{\lambda\alpha}{4\pi} \tag{2.76}$$

2.3.6 Drude-Lorentz Model:

When the electric field of the electromagnetic waves interacts with the dielectric materials, it causes dipole oscillations. The electrons bounded to the positively charged nucleuses vibrate around an equilibrium position with a specific resonant frequency according to Drude-Lorentz model.

The equation of motion (Schrödinger equation) that describes the electron motion is defined by the following:

$$m_o \frac{d^2x}{dt^2} + m_o\, \gamma\, \frac{dx}{dt} + m_o\, \omega_o^2\, x = -e\, E \tag{2.77}$$

Where m_o is the mass of the electron, x is the electron displacement, γ is the damping coefficient, ω_o is the resonant frequency, e is the charge of the electron, and E is the electric field.

The final solution becomes:

$$x(t) = \frac{-e\, E_o}{m_o(-\omega^2\, -\, i\, \omega\, \gamma\, +\, \omega_o^2\,)}\; e^{-i\omega t} \tag{2.78}$$

From the solutions of ε_{eff} the real and imaginary dielectric constants ε_1 and ε_2 is obtained as:

$$\varepsilon_1(\omega) = 1 + \chi + \frac{\mathrm{N}\, e^2}{\varepsilon_o m_o}\left(\frac{\omega_o - \omega^2}{(\omega_o^2 - \omega^2)^2 + (\gamma\omega)^2}\right) \tag{2.79}$$

$$\varepsilon_2(\omega) = \frac{\mathrm{N}\, e^2}{\varepsilon_o m_o}\left(\frac{\gamma\omega}{(\omega_o^2 - \omega^2)^2 + (\gamma\omega)^2}\right) \tag{2.80}$$

2.4 The RLC circuit

The RLC circuit is an electrical circuit that consists of resistance (R), capacitance (C), and inductance (L) which is connected in series or parallel. A voltage source is used to provide AC signals in this type of circuit. The circuit creates a harmonic oscillator for current and resonates in the same way that an LC circuit works. The resistor increases the decay of these oscillations, which is also known as damping. In addition, the resistor reduces the peak resonant frequency. The three circuit elements, R, C, and L, can be combined in a number of different topologies. All three elements in the series

or in the parallel contact are the simplest in concept and the most straightforward to analyze.

2.4.1 The series RLC circuit

The RLC series circuit has a single loop with the same instantaneous current flowing through the loop for each circuit element. The amplitude of the source voltage (V_S) is composed of the three individual element voltages $V_R, V_C \; and \; V_L$. Fig. 2.11 presented a diagram of the RLC series circuit.

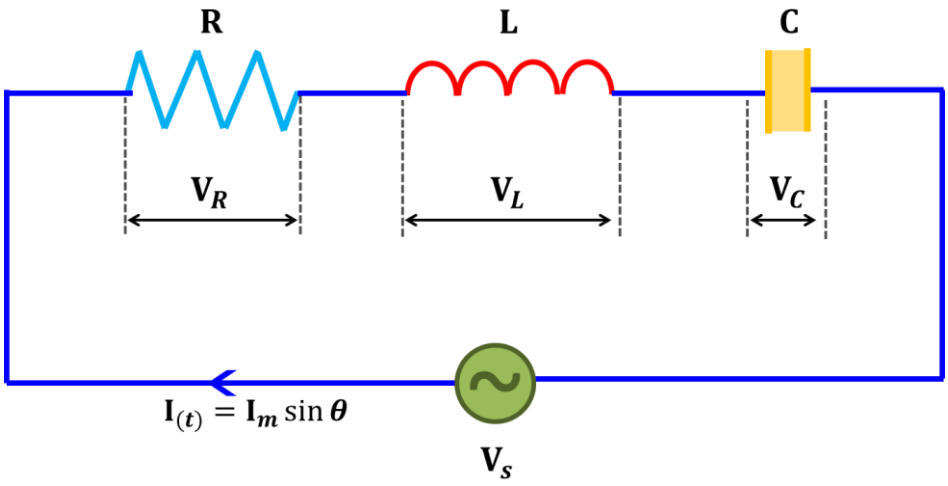

Fig. 2.11 The RLC series circuit.

The component voltages $V_R, V_L \; and \; V_C$ are given by the following equations:

$$V_R = IR \tag{2.81}$$

$$V_L = I\omega L \tag{2.82}$$

$$V_C = \frac{I}{\omega C} \tag{2.83}$$

Where R is the resistance, I is the current, ω is the source angular frequency, C is the capacitance and L is the inductance. The expression ωL is known as the inductive reactance, and it is denoted by a symbol X_L. Also, the expression $\frac{1}{\omega C}$ is known as the capacitive reactance and it is denoted by a symbol X_C. By using Kirchhoff's voltage

law (KVL), which states that around any closed loop, the sum of voltage drops around the loop equals the sum of the electromotive forces (EMF's), then the sum of the three voltages gives us the amplitude of the source voltage V_s, as:

$$V_s - V_R - V_L - V_C = 0 \tag{2.84}$$

$$V_s = IR + I\omega L + \frac{I}{\omega C} \tag{2.85}$$

Since the capacitive and inductive reactance's X_C and X_L are functions of the supply frequency, the sinusoidal response of a RLC series circuit will vary with frequency f. The individual voltage drops through each circuit element of R, C *and* L element will then be "out of phase" with each other, as described by:

$$I(t) = I_m \sin(\omega t) \tag{2.86}$$

The instantaneous voltage through a pure resistance (V_R) is "in phase" with current. Where the instantaneous voltage across a pure inductance (V_L) is "leads" the current by 90°. While the instantaneous voltage across a pure capacitance (V_C) is "lags" the current by 90°. Therefore, V_L and V_C are 180° "out-of-phase" and opposing each other. This can be seen in Fig. 2.12 for the RLC series circuit.

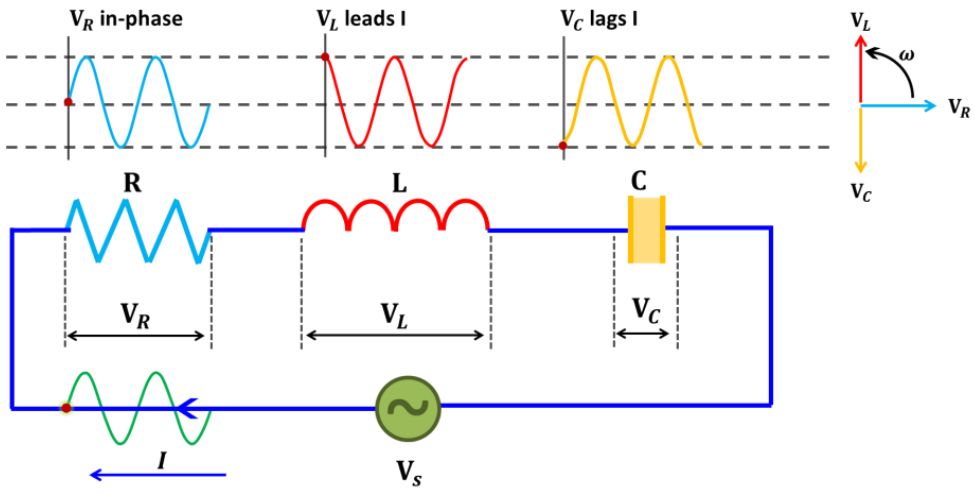

Fig. 2.12 The series RLC analysis.

As seen in the Fig. 2.13, the voltage triangle of the RLC series circuit gives that:

$$V_S^2 = V_R^2 + (V_L - V_C)^2 \tag{2.87}$$

$$V_S = \sqrt{V_R^2 + (V_L - V_C)^2} = I\sqrt{R^2 + (X_L - X_C)^2} = IZ \tag{2.88}$$

Where, $Z = \sqrt{R^2 + (X_L - X_C)^2}$ is the impedance of the circuit which is determined by the resistance (R), capacitive (X_C) and inductive (X_L) reactances. Fig. 2.13 presented the voltage phasor diagram.

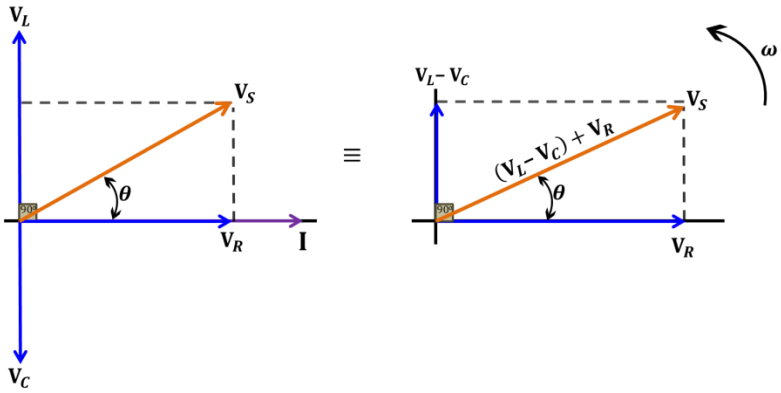

Figure 2.13. Phasor diagram of the RLC series circuit.

The amplitude of the source voltage is proportional to the amplitude of the current, with the proportionality constant known as the circuit impedance. The total impedance of the circuit is determined by the relation (2.88), which can be illustrated by an impedance triangle as seen in Fig. 2.14 below.

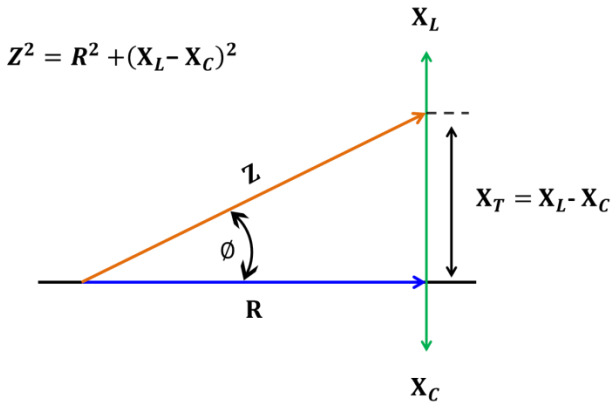

Figure 2.14. The impedance triangle of the RLC series circuit.

The phase angle θ between the source voltage V_s and the current I is the same as the angle (ϕ) between the impedance Z and the resistance R in the impedance triangle. This phase angle can be positive or negative in value depending on whether the source voltage leads or lags the circuit current and can be determined mathematically from the ohmic values of the impedance triangle as:

$$cos\phi = \frac{R}{Z} \qquad sin\phi = \frac{X_L - X_C}{Z} \qquad tan\phi = \frac{X_L - X_C}{R} \tag{2.89}$$

2.4.2 The reflection coefficient and return loss:

The impedance spectra were used to determine the magnitude of propagating signal reflectivity $|\Gamma| \equiv \rho$. The calculated reflection coefficient can be used to determine the performance of the pn devices as wave traps. The reflection coefficient ρ is measured from the relation:

$$\rho = \left|\frac{Z_L - Z_S}{Z_L + Z_S}\right| \tag{2.90}$$

where L is the load, and S is the source, thus, Z_L being the impedance of the sample and Z_S is the impedance of the source [48]. The standard evaluation procedure for this parameter shows that the value of -1 appears when the device exhibits shorts, still negative when the load impedance is less than that of source, and becomes positive when the load impedance is greater than that of source. If there is no match between source and load (device), the ρ value is one which indicates an open load. The value +1 means all incident waves are rejected, and the value of zero means all waves are transmitted, which indicates a perfect match.

The trapped wave quality of the signal is detected from the return loss spectra. The return loss L_r is measured by the relation:

$$L_r = -20\ log(\rho) \tag{2.91}$$

The higher the return loss value $L_r > 20\,dB$, the more qualitative the wave trap. In communication engineering, return loss refers to the loss of power in the signal rejected by a discontinuity in devices under test.

Filters are circuits that can be designed to modify, reshape, or reject unwanted frequencies of an electrical signal or accept and pass those signals wanted by the circuit designer. Thus, filters are needed in variable frequency supply circuits. The specific type of filter can be determined from the reflection coefficient and return loss values.

2.4.3 Alternating current and conduction mechanisms in solids:

The alternating current (AC) conductivity spectra can be governed by quantum mechanical tunneling (QMT) or correlated barrier hopping conduction (CBH) or may both of them [49]. Conductivity can be obtained from the conductance (G) using the following relation:

$$G = \sigma . \frac{A}{l} \tag{2.92}$$

Where G is the measured conductance, σ is the conductivity, A is the cross sectional area and l is the length of the conductor.

Early published theories [49] assume that the frequency dependence of the AC conductivity is expressed by the equation:

$$\sigma_{AC}(\omega) = A\,\omega^{s} \tag{2.93}$$

Where A is a constant depends on temperature, $\omega = 2\pi f$ is the angular frequency of the applied AC field, and s is the frequency exponent parameter that is generally less than or equal to unity $(0 \leq s \leq 1)$. This form of the conductivity equation (2.93) appears if the mechanism of loss has a wide range of relaxation times (τ). The exponent value $s = 1$ is found if the distribution of relaxation times $(n(\tau))$ is

inversely proportional to τ. Under this condition, the relaxation time (τ) is given by the equation:

$$\tau = \tau_o \, e^{\xi} \tag{2.94}$$

where ξ is a random variable, τ_o is characteristic relaxation time often taken to be the inverse of the phonon frequency (ν).

In the case where QMT dominates $\xi = 2\alpha R$ with R refering to the intersite separation and α is spatial decay parameter for the wave functions which is employed to represent the localized state at each site. α is approximately, α constant for all sites and equal $0.1\ A^{\circ}$ [50]. For an electron undergoing quantum mechanical tunnelling, the AC conductivity can be described by the equation [49]:

$$\sigma_{TUN}(\omega) = \frac{\pi^4 \, e^2 \, K \, T \, \alpha^{-1} \big(N(E_F)\big)^2 \, \omega \, R_\omega^2}{24} \tag{2.95}$$

In this equation, $N(E_F)$ is the density of localized states near the Fermi level (assumed constant with varying frequency) and R_ω is the hopping distance at a particular frequency (ω). R_ω is given by:

$$R_\omega = \frac{1}{2\,\alpha} \ln\left(\frac{1}{\omega \, \tau_o}\right) \tag{2.96}$$

The frequency dependence of $\sigma(\omega)$ in the equation (2.93) can be used to execute the derivative s. Taking the logarithm for both sides of the equation (2.93) becomes:

$$\ln \sigma(\omega) = \ln A \; + s \; \ln(\omega) \tag{2.97}$$

Executing the derivatives for each side:

$$d \ln \sigma(\omega) = 0 \; + s \; d \ln(\omega) \tag{2.98}$$

From equation (2.98) we conclude that the exponent s can be found from the relation:

$$s = \frac{d \ln \sigma(\omega)}{d \ln(\omega)} \tag{2.99}$$

For the QMT model, s is given by:

$$s = 1 - \frac{4}{\ln\left(\frac{1}{\omega\, \tau_o}\right)} \tag{2.100}$$

As a result, for the QMT model, the frequency exponent s is frequency dependent and decreases with increasing frequency at constant temperature. On the other hand, the CBH theory assumes that $\xi = \frac{W_h}{K\,T}$ with W_h being the hopping barrier height, for this case, as long as the frequency of the signal that propagates is less than the charge of the carrier jump frequency, the AC conductivity will increase with that frequency [49]. The AC conductivity of CBH can be calculated using the following equation:

$$\sigma_{CBH}(\omega) = \sigma_H(\omega) + \frac{[\sigma_L(\omega) - \sigma_H(\omega)]}{(1 + \omega^2\tau^2)} \tag{2.101}$$

Where, the subscript symbols H and L represent conductivity values at high and low frequencies, respectively.

As previously mentioned, it is possible that the AC conductivity corresponds to the domination of the two conduction mechanisms, QMT and CBH, as presented by the relation:

$$\frac{1}{\sigma_{total}} = \frac{1}{\sigma_{QMT}} + \frac{1}{\sigma_{CBH}} \tag{2.102}$$

Where, σ_{total} is the total conductivity, σ_{QMT} is the conductivity resulted from quantum mechanical tunnelling and σ_{CBH} is the conductivity resulted from correlated burrier hopping conduction.

2.4.4 Alternating current and Capacitance mechanisms in solids:

Here we consider the Ershov model [49] for the negative capacitance effect (NC). It shows the effect of negative capacitance in terms of time range transient currents in response to small voltage signals. Ershov assumed that introducing a phase or pulsed voltage would lead to an instantaneous change in charges on the contacts. According to this approach, the total capacitance $(C(\omega))$ consists of geometric part (C_o) and relaxation part (C_1) [49]. C_1 was found to be caused by the impact ionization, trapping, electron transport and other physical process [49]. Ershov's theorems arrived at the conclusion of Jonscher, which states that the source of NC is related to the positive or nonmonotonic behaviour of the derivative of the transient current $(j(t))$ in response to a small voltage phase. Using this approach, which is dependent on the charge of nonmonotonic or monotonic variations, Qasrawi et al [49] consider the existence of two different frequency domains $(\omega - \omega_p)$ and $(\omega - \omega_n)$ where ω_p and ω_n are the limits of frequency domains in the p and n regions, respectively. As a result of Ershov's equation, which has the following form:

$$C_1 = \frac{\Delta Q}{\Delta V} \tag{2.103}$$

$$C_1 = \frac{1}{\Delta V}\int_0^{\infty} \delta_j(t)\cos\omega t \; dt \tag{2.104}$$

$$C_1 = \frac{1}{\omega\Delta V}\int_0^{\infty} \left(-\frac{d\delta_j(t)}{dt}\right)\sin\omega t \; dt \tag{2.105}$$

It can be rewritten as:

$$C_1 = \frac{1}{\Delta V}\int_0^{\infty} \delta_j(t)\cos\left(\omega - \omega_{n,p}\right)t \; dt \tag{2.106}$$

$$C_1 = \frac{1}{\omega\Delta V}\int_0^{\infty} \left(-\frac{d\delta_j(t)}{dt}\right)\sin\left(\omega - \omega_{n,p}\right)t \; dt \tag{2.107}$$

Where ΔQ is the charge. ΔV is the voltage, $\omega_n$and ω_p as previously defined and $\delta_j(t)$ is the time domain behaviour of the transient current. If $\delta_j(t)$ is positive and monotonically decreases to Zero as t goes to ∞, then $C_1 > 1$ and $C(w) > C_o$ at any frequency. The Ershov approach also assumes [49]:

$$\delta_j(t) = \Delta V \left[a_n \, e^{\frac{-t}{\tau}} - a_p \, e^{\frac{-t}{\tau}} \right] \tag{2.108}$$

Where a_n and a_p are fitting parameters for the dielectric (capacitance) response in F/s. It represents the rate of change of dynamic capacitance with time:

$$\frac{d\delta_j(t)}{dt} = \Delta V \left[\frac{-a_n}{\tau_n} \, e^{\frac{-t}{\tau_n}} + \frac{a_p}{\tau_p} \, e^{\frac{-t}{\tau_p}} \right] \tag{2.109}$$

Where τ_n and τ_p represent the relaxation time of electrons and holes, respectively.

Substituting equation (2.108) in the equation (2.109):

$$C_1 = \frac{1}{\omega \Delta V} \int_0^{\infty} - \left(\Delta V \left[\frac{-a_n}{\tau_n} \, e^{\frac{-t}{\tau_n}} + \frac{a_p}{\tau_p} \, e^{\frac{-t}{\tau_p}} \right] \right) \sin(\omega - \omega_{n,p}) t \; dt \tag{2.110}$$

$$C_1 = \frac{1}{\omega} \int_0^{\infty} \left(\frac{a_n}{\tau_n} \, e^{\frac{-t}{\tau_n}} \sin(\omega - \omega_n) t \; dt - \frac{a_p}{\tau_p} \, e^{\frac{-t}{\tau_p}} \, \sin(\omega - \omega_p) t \; dt \right) \tag{2.111}$$

$$C_1 = \frac{a_n}{\omega \tau_n} \int_0^{\infty} e^{\frac{-t}{\tau_n}} \sin(\omega - \omega_n) t \; dt - \frac{a_p}{\omega \tau_p} \int_0^{\infty} e^{\frac{-t}{\tau_p}} \, \sin(\omega - \omega_p) t \; dt \tag{2.112}$$

By using Fourier integral form:

$$\sqrt{\frac{2}{\pi}} \int_0^{\infty} f(t) \sin kt \; dt = F_s(k) \tag{2.113}$$

Then:

$$f(t) = \sqrt{\frac{2}{\pi}} \int_0^{\infty} F_s(k) \sin kt \; dt \tag{2.114}$$

In our case, $k = \omega - \omega_n$, $a = \frac{1}{\tau_n}$ and $f(t) = e^{\frac{-t}{\tau_n}}$, the integrated equation (2.113) becomes:

$$f(\omega - \omega_n) = \sqrt{\frac{2}{\pi}} \int_0^\infty e^{\frac{-t}{\tau_n}} \sin(\omega - \omega_n)t \; dt \tag{2.115}$$

From Fourier integral tables, for $f(t) = e^{-at}$ and by substituting in equation (2.113) $F_s(k) = \sqrt{\frac{2}{\pi}} \frac{k}{(a^2+k^2)}$, then equation (2.113) becomes:

$$\sqrt{\frac{2}{\pi}} \int_0^\infty e^{-at} \sin kt \; dt = \sqrt{\frac{2}{\pi}} \frac{k}{(a^2 + k^2)} \tag{2.116}$$

Divided both sides by $\sqrt{\frac{2}{\pi}}$:

$$\int_0^\infty e^{-at} \sin kt \; dt = \frac{k}{(a^2 + k^2)} \tag{2.117}$$

$$\int_0^\infty e^{\frac{-t}{\tau_n}} \sin(\omega - \omega_n)t \; dt = \frac{\omega - \omega_n}{\left(\left(\frac{1}{\tau_n}\right)^2 + (\omega - \omega_n)^2\right)} \tag{2.118}$$

Substituting equation (2.118) in the equation (2.112):

$$C_1 = \frac{a_n}{\omega\tau_n} \frac{\omega - \omega_n}{\left(\left(\frac{1}{\tau_n}\right)^2 + (\omega - \omega_n)^2\right)} - \frac{a_p}{\omega\tau_p} \frac{\omega - \omega_p}{\left(\left(\frac{1}{\tau_p}\right)^2 + \left(\omega - \omega_p\right)^2\right)} \tag{2.119}$$

$$C_1 = \frac{a_n \, \tau_n(\omega - \omega_n)}{\omega(1 + (\omega - \omega_n)^2 \, \tau_n^2)} - \frac{a_p \, \tau_p\left(\omega - \omega_p\right)}{\omega\left(1 + \left(\omega - \omega_p\right)^2 \tau_p^2\right)} \tag{2.120}$$

But $\omega \gg \omega_{n,p}$, so the equation (2.120) becomes:

$$C_1 = \frac{a_n\,\tau_n\,\omega}{\omega(1+(\omega-\omega_n)^2\,\tau_n^2)} - \frac{a_p\,\tau_p\,\omega}{\omega\left(1+\left(\omega-\omega_p\right)^2\,\tau_p^2\right)} \tag{2.121}$$

$$C_1 = \frac{a_n\,\tau_n}{1+(\omega-\omega_n)^2\,\tau_n^2} - \frac{a_p\,\tau_p}{1+\left(\omega-\omega_p\right)^2\,\tau_p^2} \tag{2.122}$$

Then the equation of the total capacitance [49], becomes:

$$C(\omega) = C_o + \frac{a_n\,\tau_n}{1+(\omega-\omega_n)^2\,\tau_n^2} - \frac{a_p\,\tau_p}{1+\left(\omega-\omega_p\right)^2\,\tau_p^2} \tag{2.123}$$

Chapter Three

Experimental details

Thin film preparation plays a vital role in producing heterojunction devices. Many procedures could be used to prepare a heterojunction thin film device. The thermal vapor deposition technique was used in this work. The details of producing the devices are shown in this chapter.

3.1 Substrate cleaning

Glass slides (7.5 cm length and 0.2 cm thickness) were cleaned before use in the preparation process of the films. Firstly, some of the glasses are divided equally into small pieces of 2.5 cm by a glass cuter. The glasses were then manually cleaned with a softening sponge, dish-washing liquid, distilled water and alcohol. Then, the cleaned glasses were inserted in a beaker filled with Ethyl-alcohol (70%) and covered with aluminium foil. To crack proteins that are expected to be stuck onto the glass, the beaker was heated for 15 minutes. After that, they were ultrasonically cleaned at 70^{o} for 20 minutes. Then, they were washed with alcohol and dried. Finally, we get sure that the glasses do not have any scratches and/or cracks on their surface and then we use them as clean substrates for our work.

3.2 Heater preparation.

Quartz tubes inserted into heating crucible were used due to its ability to hold out the powders. The powders can melt inside it to form bulk alloy material and it can be deposited at the same time. Installing and using this type of evaporation sources needs a special holder, which was smelted and shaped to match with our evaporator system. Fig. 3.1 shows the glass tube and its holder.

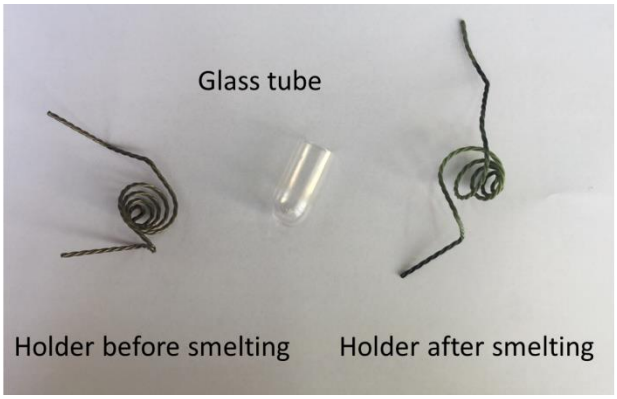

Figure 3.1. The glass tube preparation.

3.3 Deposition process and thin film preparation.

In this part, the thermal vapor deposition technique was applied four times to form our heterojunction films under a vacuum pressure of ~1×10^{-4} mbar. Fig. 3.2 shows the VCM 600 thermal vacuum evaporator system. In the first run, the cleaned glass substrates in addition to Al and Ag substrates were fixed close to each other on a metal plate (substrate holder). Teflon tape is used to cover a small area (about 2 mm) on the edges of metals (Al and Ag) substrates before evaporating Aluminium-antimony (Al-Sb). Then, 0.2 gm of high purity Aluminum tiny pieces (99.999% Alfa Aesar) and 0.2 gm of high purity Antimony powder (99.999% Alfa Aesar) were weighed, mixed and put in a glass tube (Item 2, Fig. 3.2). Then we closed the bell jar and turned on the evaporation system. When the vacuum pressure reached 1.1×10^{-4} mbar, we started the evaporation mechanism and opened the shutter after 5 minutes at a current value of 50 A, a deposition rate of 43 A/s and at a temperature of 626^{o} C were monitored. A layer of thickness 503 nm Al-Sb alloy films were deposited onto the glass, Al and Ag substrates. The thickness was monitored via an INFICON STM-2 thickness monitor. The produced films and the remaining solid bulk which was melt in the tube were maintained inside the jar until the champer cooled down.

Figure 3.2 The VCM 600 evaporation set up.

In the second run, the same procedure was repeated but we reduced the amount of aluminium compared to the antimony amount, in order to obtain optical properties. In this run, 0.054 gm of Al and 0.216 gm of Sb were mixed and evaporated under the same vacuum conditions. A layer of 130 nm Al-Sb films were deposited on the glass and ITO substrates. Aluminium foil was used to cover one third of the surface of some produced samples to execute the third run in the evaporation system. The solid orange CdS stone was crushed into lumps with the help of crystals mortar and pestle agate (Inset of Fig. 3.3). The powders were then placed in a tungsten heater of boat shape.

Figure 3.3. The setup of the evaporation process for the third and fourth runs.

A 0.35 gm of Cadmium Sulfide (99.999%) was used to evaporate CdS onto glass, ITO, glass/AlSb and ITO/AlSb substrates. The recorded thickness was on the order of 270 nm. In this cycle, the CdS pellets jumped and escaped from the CdS boat. So, the third run was repeated to obtain the desired thickness. Again, a 0.4035 gm large piece with CdS lumps were placed on the CdS boat, before the fourth run (Inset of Fig. 3.3). When the pressure reaches 4.9×10^{-4} mbar, the vaporization process begins, and the current is gradually increased to avoid jumping pellets. A 540 nm-thick CdS was deposited (in the last two runs). Finally, the desirable films were produced by evaporating CdS on Al-Sb layer using the (PVD) technique to prepare a hetrojunction device. To produce an electronic device, the ITO metal edges were needed, the ITO-substrates with the help of Carbon (C) and Silver (Ag) circular points above the CdS film. The geometrical design and the final AlSb/CdS heterojunction films of the samples are shown in Fig. 3.4. The optical images of the real samples are shown in Fig. 3.5.

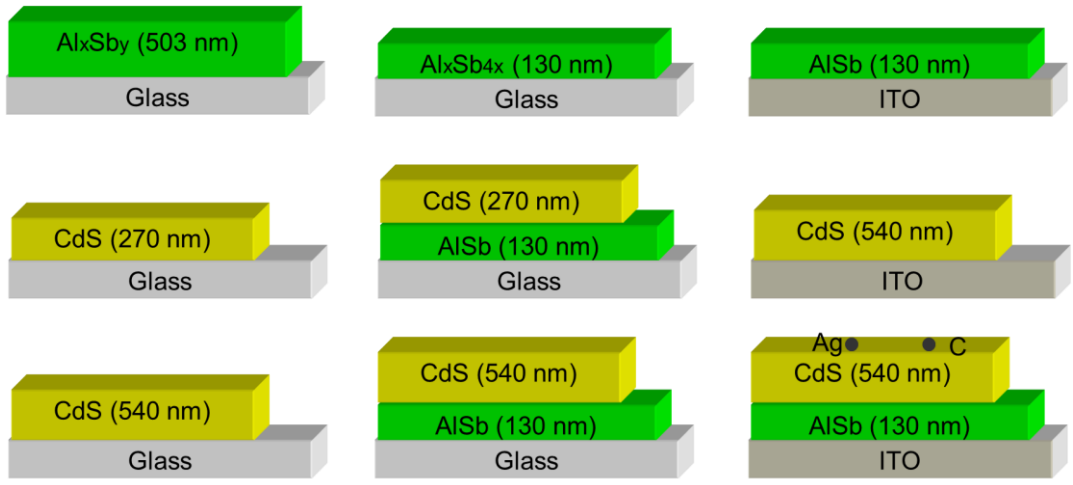

Figure 3.4. The geometrical design of glass/AlSb, glass/CdS, glass/AlSb/CdS, ITO/AlSb, ITO/CdS and ITO/AlSb/CdS heterojunction samples.

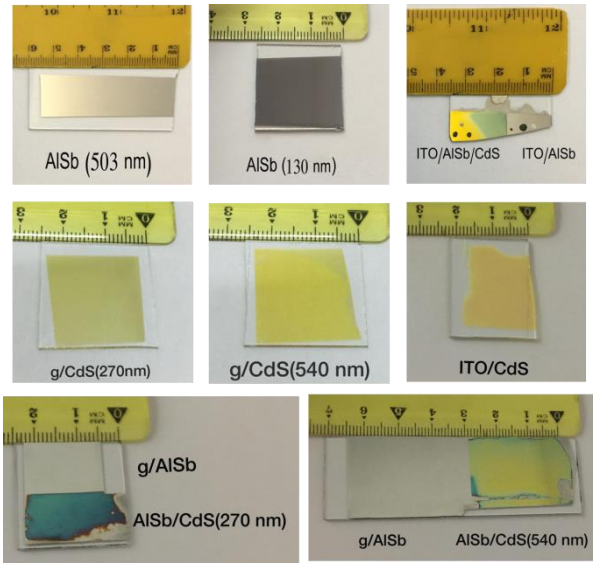

Figure 3.5. The optical images of the real samples of glass/AlSb, glass/CdS, glass/AlSb/CdS, ITO/AlSb, ITO/CdS and ITO/AlSb/CdS.

3.4 Bulk analysis

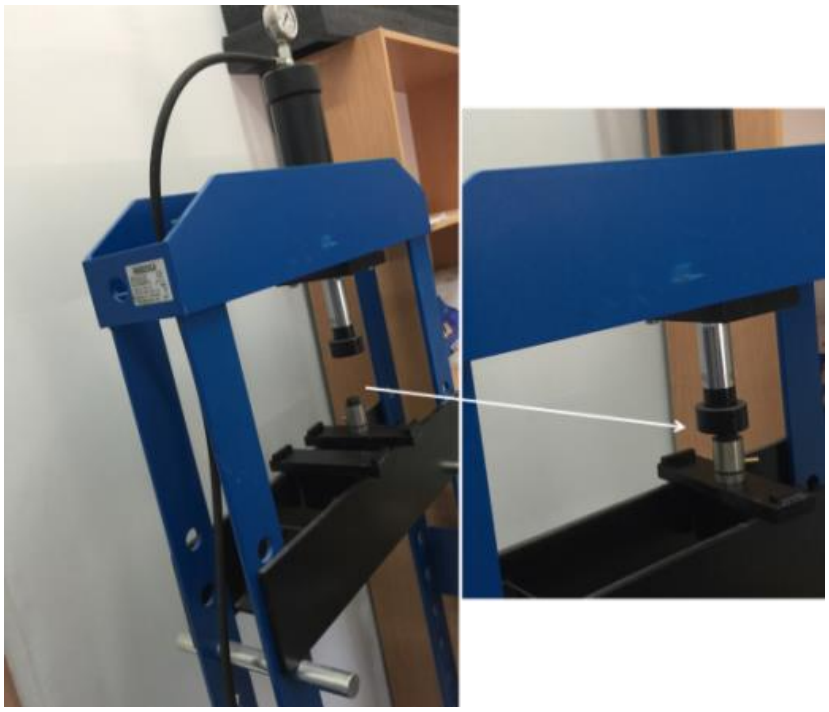

Figure 3.6: The piston and the press machine of bulk.

The Al_x-Sb_y solid bulk which remained after the powders were molten, which was produced in the first run with an irregular shape, was subjected to a pressure of approximately 100 bar with the help of the piston as shown in Fig. 3.6, to obtain a

disk shape with two semi-flat faces (brown and white faces) as shown in Fig. 3.7. The structural and electrical properties of the obtained AlSb bulk are studied with various measuring techniques such as X-ray diffraction (XRD) and impedance spectroscopy technique.

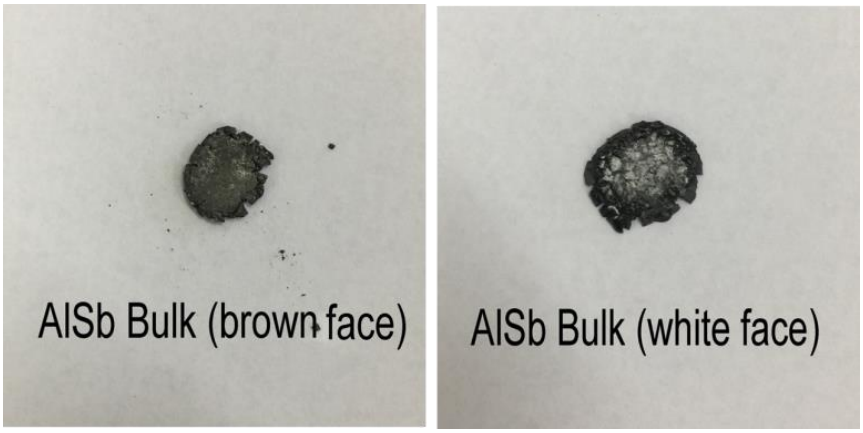

Figure 3.7: The two faces of the pressed AlSb bulk.

3.5 Thin films analysis

In order to study the structural, optical and electrical properties, the fabricated AlSb/CdS and ITO/AlSb/CdS heterojunction films were carried out with various measuring techniques such as, X-ray diffraction (XRD), optical spectrophotometry and impedance spectroscopy technique.

3.5.1 The X-ray diffraction measurements for bulk and thin film samples.

The crystalline structure of both faces of the AlSb bulk and the X-ray diffraction patterns of the produced thin films were characterized by means of Rigaku MiniFlex 600 X-ray diffractometer. Fig. 3.8 displayed the X-ray diffractometer with K_{α} radiation of a Copper anode emitting XRD of an average wavelength of 1.5418 Å at

40 KV and 15 mA. The X-ray diffractometer registered the intensity as a function of angle (2θ). The diffraction angle 2θ was set between 10^{o}-80^{o}, with a scan speed of 1 deg/min. The data was collected by using the MiniFlex support program that is connected with the X-ray diffractometer.

Figure 3.8: Rigaku MiniFlex 600 X-ray diffractometer.

3.5.2 The optical measurements for thin film samples.

The optical measurements of AlSb (130 nm), CdS (540 nm), AlSb/CdS samples were recorded with the help of Thermo Scientific Evolution 300 Ultra Violet visible light spectrophotometer. The optical data of transmittance (T %) and reflectance (R %) spectra were measured in the range of wavelength (300-1100 nm). The measurements were obtained at a normal incidence angle of 15^{o} and the scanning speed of 1200 nm/min. The data was collected and analyzed by using the Vision Pro software program, which was attached to the system as shown in Fig. 3.9. The data was applied and processed to investigate some optical parameters like absorption coefficient (α), interband transition energies (E_e), band tail energies, energy band gaps (E_g), and the dielectric constant (ε).

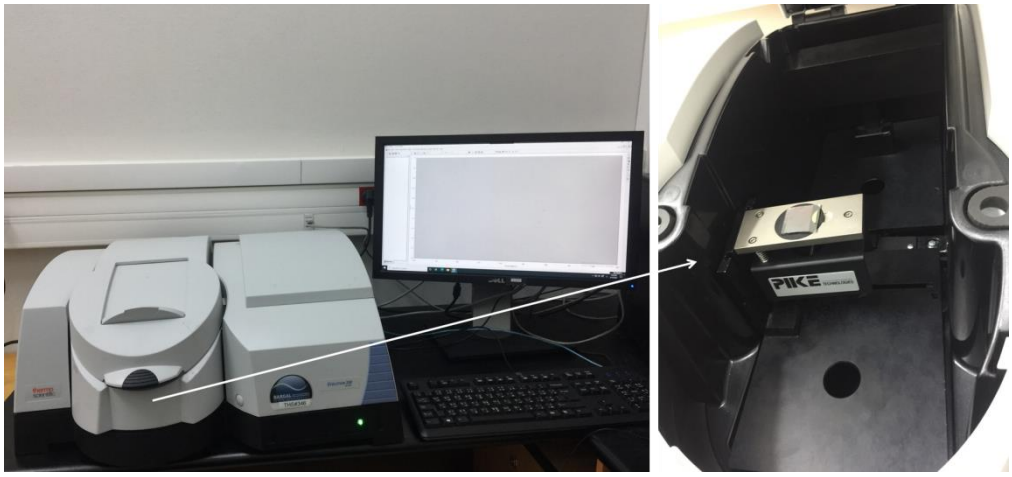

Figure 3.9: The UV-VIS spectrophotometer.

3.5.3 The impedance measurements for bulk and thin film samples.

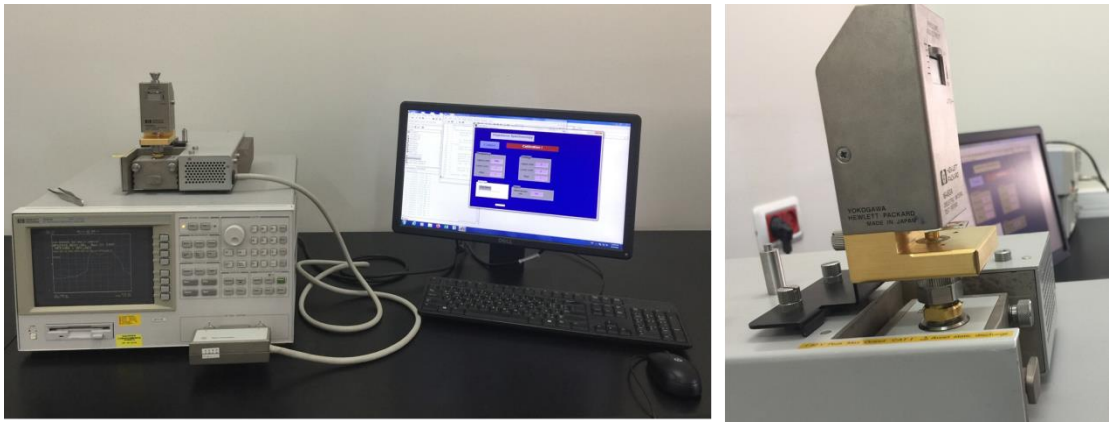

Figure 3.10: Agilent 421BRF signal generator impedance analyzer spectrometer setup.

Agilent 421BRF signal generator impedance analyzer (10-1800 MHz) spectrometer is used to measure the impedance of the bulk and heterojunction thin films. The data was measured in the frequency range of 10-1800 MHz. The data was taken by the MATLAB software connected with the impedance spectrometer unit, which is shown in Fig. 3.10. The films were conducted with the help of a dielectric fixture. The impedance (Z), resistance (R), inductance (L), reactance (X), conductance (G), capacitance (C) and reflection coefficient (ρ) were computed and listed in the same

system. To measure the mentioned parameters, the film (ITO/AlSb/CdS) was contacted manually with Carbon (C) circular points as we mentioned before. The test of AlSb bulk was performed with the help of a dielectric fixture.

3.5.4 The Hot-Probe technique for thin film samples.

The hot-probe technique is used to test the conductivity type of the semiconductors, which is needed in many procedures. The setup of this technique required contacting the produced sample with a heat soldering iron (hot probe) and a cold probe, as displayed in Fig. 3.11. Both probes are connected by the digital multi-meter (DMM). While the hot iron was wired to the positive terminal of the DMM, the cold iron was wired to the negative terminal. When the voltage reading of (DMM) is positive, then the semiconductor is n-type. While the p-type semiconductor displays a negative voltage reading. While the hot-probe technique raveled p-type of conduction for the AlSb layer, the CdS layer exhibited n-type of conduction.

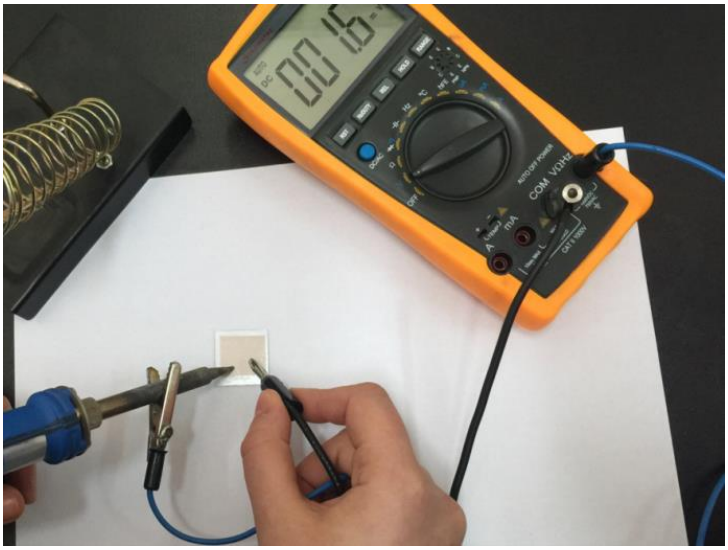

Figure 3.11: The hot-probe technique.

Chapter four

Results and discussions

4.1 Structural analysis

4.1.1 Structural analysis of AlSb films

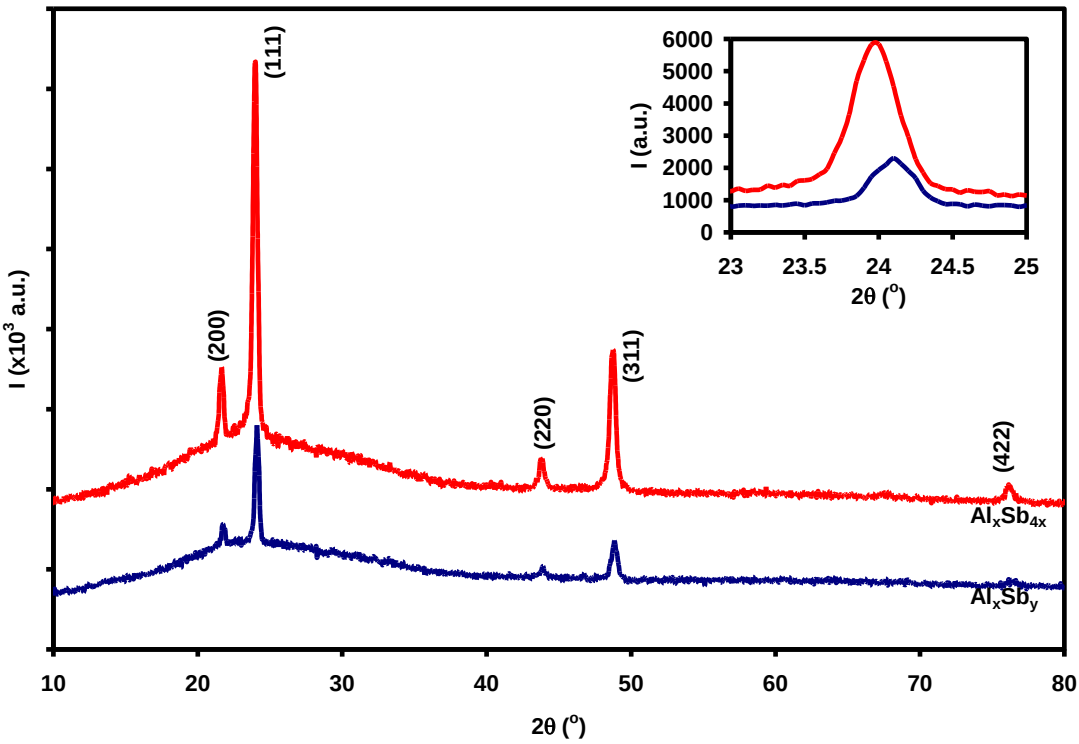

Figure 4.1. The X-ray diffraction patterns for the Al_xSb_y and Al_xSb_{4x} alloy films. The inset shows the maximum peak of the samples.

The XRD patterns for the Al_xSb_y and Al_xSb_{4x} alloy films which are grown onto glass substrates are shown in Fig. 4.1. As seen from the figure, the two films exhibit the same intensive peaks with a shift in the position of the diffraction angles (2θ). It is also observed that, XRD patterns resulting from Al_xSb_{4x} film are more intensive than the Al_xSb_y film. As the inset of Fig. 4.1 shows, the intensity of the major peak increased from 2300 to 5836 (a.u). The sharp XRD patterns of the studied samples which are analyzed with the help of "TREOR 92" and "Crystdiff" software packages

reveal peaks that are related to zinc blende cubic aluminum antimonide (AlSb) being best oriented along the (111) direction with lattice constants of 6.126 Å.

In order to understand the difference in the structural characteristics of the Al_xSb_y and Al_xSb_{4x} samples. The crystallite size (*D*), micro-strain (ε), defect density (δ) and stacking faults percentage (*SF %*) are calculated with the help of equations (2.15-2.18). The values of the structural parameters are illustrated in Table 4.1. It is clear from the table that the increasing amount of antimony compared to aluminum highly increased the intensity, indicating a better crystallization process in the alloy film as we mentioned before. For the Al_xSb_y and Al_xSb_{4x} structures, the lattice parameter of Al_xSb_{4x} is larger than that previously reported for Al_xSb_y.

Table 4.1. The structural parameters of Al_xSb_y and Al_xSb_{4x} alloy films of the main peak.

Sample	**Al_xSb_y**	**Al_xSb_{4x}**
2θ (^{o})	24.1	24.0
I (a.u.)	2300	5836
d (A^o)	3.69	3.71
(hkl)	(1 1 1)	(1 1 1)
a (A^o)	6.39	6.42
D (nm)	24	21
SF (%)	0.33	0.38
ε(x10^{-3})	7.15	8.21
δ(x10^{12} lines/cm^2)	6.9	9.0

As illustrated in Table 4.1, while the grain size (*D*) of Al_xSb_{4x} revealed a smaller value, the stacking faults (*SF %*), microstrain (ε) and dislocation density (δ) revealed a higher values than that listed for Al_xSb_y. The most pronounced effect of the non-stoichiometric composition of AlSb is readable from the defect density. The defect density of Al_xSb_y is increased by 30.4% when Sb content is increased 4 times (y = 4x). Additional tests like energy dispersion x-ray spectroscopy is needed to determine

to what degree Al is deficient in the films. Defects are usually formed by melt pool discontinuities and lack of melt pool overlap [51]. Surface defects are also formed during the high temperature preparation of the samples owing to the formation of schottky defects in the bulk which give rise to a none stoichiometric surface regions.

4.1.2 Structural analysis of AlSb melts

The XRD analyses of the diffraction patterns for the brown and white faces of the remaining melt (bulky sample) of Al_xSb_y are shown in Fig. 4.2 and Fig. 4.3, respectively. It is noticeable that both faces revealed a polycrystalline nature of growth. The analysis of the sharp patterns of XRD data in accordance with "crystdiff" software packages has shown that the two faces of the bulk form reveal peaks that are assigned to zinc-blende cubic aluminum antimonide and probably minor phases of the (rhombohedral) trigonal (a=4.308, b=4.308, and c=11.274 Å) antimony, face centered cubic (a = 4.034 Å) aluminum, trigonal (a=4.755, b=4.755, and c=12.991 Å) aluminum oxide and cubic (a = 11.151 Å) antimony trioxide.

The diffraction peaks of the bulk exhibit lattice parameters with remarkable differences between brown and white faces. For AlSb bulk (brown and white faces), the best oriented peak is in the (111) direction, with the diffraction angles of $2\theta=25.55^{o}$ and $2\theta=25.7^{o}$, respectively. The miller indices of the observed peaks and the calculated lattice parameters, are slightly consistent with the thin films and also consistent with literature data [52]. While the maximum peak intensity of a brown face is 3204 (a.u.), the maximum peak intensity of the white one is 1213 (a.u.).

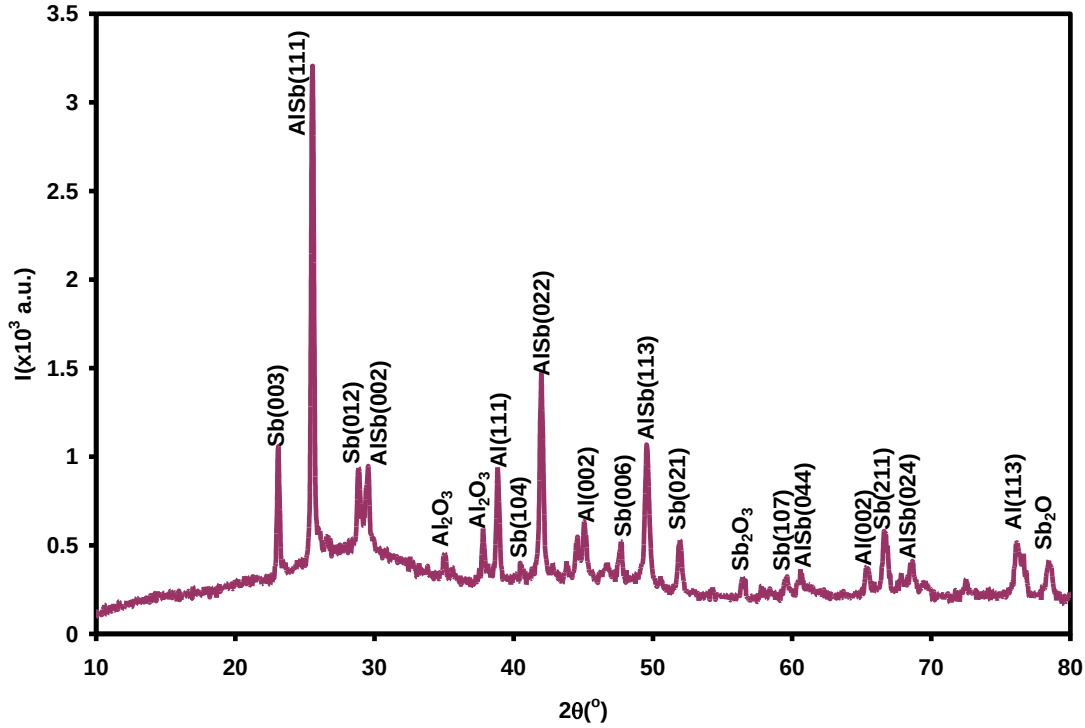

Figure 4.2. The X-ray diffraction patterns for AlSb brown face bulk.

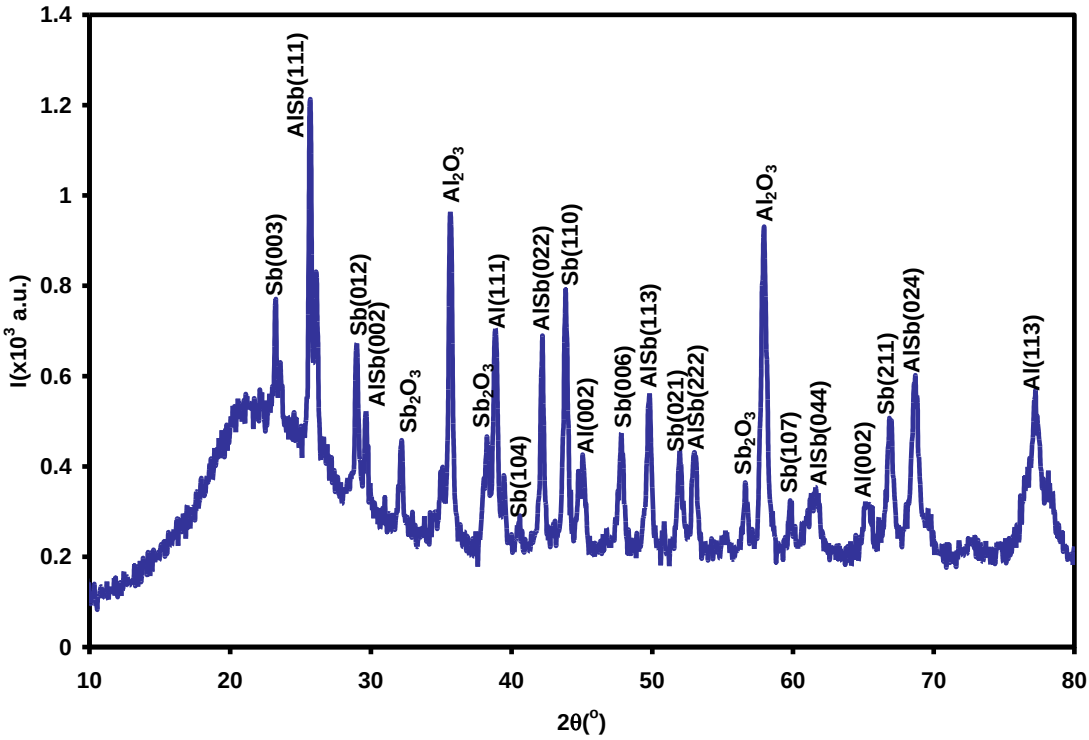

Figure 4.3. The X-ray diffraction patterns for AlSb white face bulk.

The calculated grain size (D), micro-strain (ε), defect density and stacking faults using the equation (2.15-2.18) reveled values shown in Table 4.2. As shown in Table 4.2, although the white face of the bulk form has a larger crystallite size value, the lattice constant, stacking faults (*SF*), strain (ε) and defect density (δ) achieved higher values than that tabled for the brown face. The difference between the two faces could be assigned to the mixing between the metals and alloy inside the melt. From the calculation of the phase weight of AlSb alloy in each face, we reveal the phase weight value of 42.93% for brown face, and the value of 32.02% for white face. It means that the metals has not lost in the melt and probably a small percentage of the new material (alloy) is formed.

Table 4.2. The structural parameters of AlSb brown and white face bulk are obtained from the maximum peak FWHM.

Sample	**AlSb bulk (BF)**	**AlSb bulk (WF)**
2θ (^{o})	25.55	25.7
I (a.u.)	3204	1213
d (A^o)	3.49	3.47
(hkl)	(1 1 1)	(1 1 1)
a (A^o)	6.04	6.00
D (nm)	28	34
SF (%)	0.28	0.23
ε(x10^{-3})	5.77	4.78
δ(x10^{12} lines/cm^2)	5.1	3.5

* BF: brown face and WF: white face

4.1.3 Structural analysis of AlSb/CdS heterojunctions

The x-ray diffraction (XRD) patterns for AlSb, CdS and AlSb/CdS thin films are presented in Fig. 4.4. The figure displays a polycrystalline nature for all films. As it is shown in Fig. 4.4, for AlSb substrate we observed five peaks located at 21.65^o, 24.00^o, 43.85^o, 48.75^o and 76.15^o. For CdS film, five peaks existing at 24.20^o, 25.10^o,

26.75°, 28.25° and 43.75° are detected. For a AlSb/CdS heterojunction, we also observed five peaks situated at 21.55°, 23.85°, 26.65°, 43.90° and 48.55°. As can be seen from the figure, some of the AlSb/CdS peaks were observed for AlSb substrate appeared again and the others were concerned for CdS film. The analysis of the X-ray diffraction patterns which are subjected to "TREOR 92" and "crystaldiff" software package analysis of main intensive peaks reveals cubic structure for AlSb, and a hexagonal type of structure for CdS. A peak of maximum height of AlSb film is oriented in the (111) direction at 24.00°. The main peak of the CdS film is oriented in the (002) direction at 26.75°, a peak of minor height is oriented in the (100) direction at 25.1°. The most intensive peak of AlSb/CdS heterojunction is located at 23.85°.

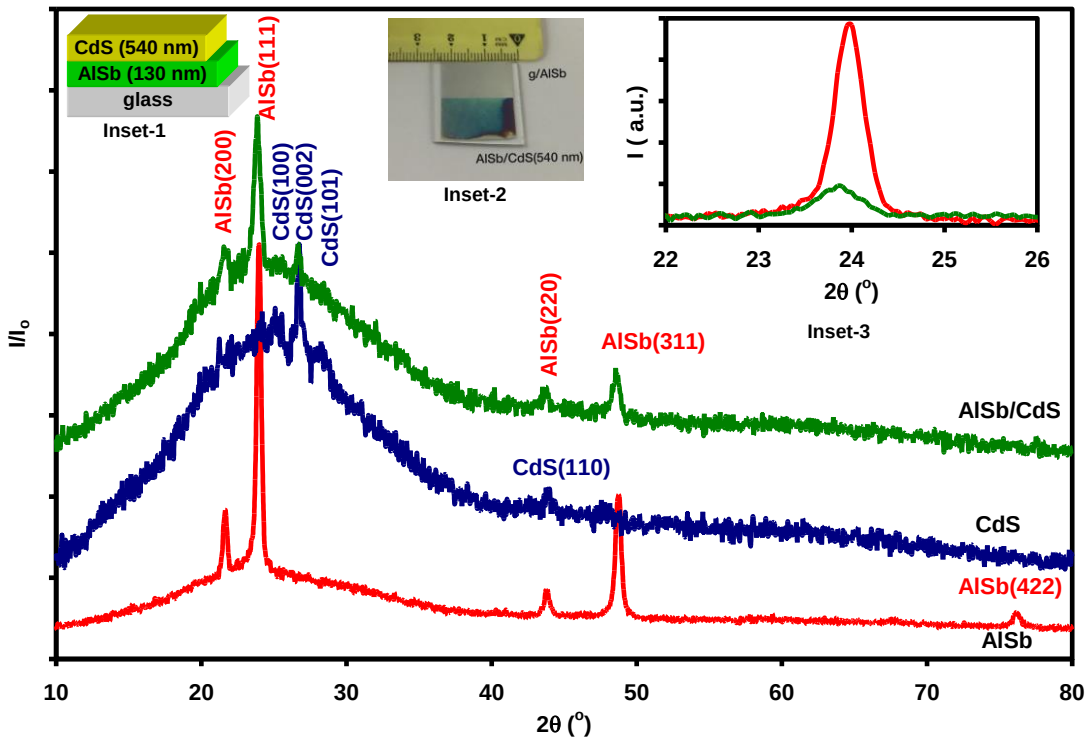

Figure 4.4. The X-ray diffraction patterns for AlSb, CdS and AlSb/CdS films. Inset-1 shows the geometrical design of the final measured sample. Inset-2 shows the optical image of the final sample. Inset-3 shows the CdS slab effect on the main reflection peak.

It is clear from the inset of Fig. 4.4, that the coating of CdS to AlSb film shifts the maximum peak position from 24.00^{o} to 23.85^{o}. The same behavior is observed for other minor peaks of the AlSb. The shift in the maximum peak position toward smaller angles is assigned to the ionic radius of cations [53]. Moreover, we observed the appearance of a peak in AlSb/CdS layer which is assigned to CdS and it is position is shifted to 26.65^{o} position. In addition, the coating of CdS resulted in a sharp decrease of the XRD intensity and causes broadening and shift in the peaks positions. The significant decrease in the intensity of X-ray patterns is accompanied with the formation of nonuniform strains and/or plastic deformations [54]. The lattice parameters (a and c) for the studied films are determined with help of the equation, (2.19) for AlSb, AlSb/CdS and equation, (2.20) for CdS maximum peak. The structural parameters values are presented in Table 4.3. The lattice parameter of AlSb is a = b = c = 6.42 A^{o}. This value is close to that we previously observed in literature data for the AlSb alloy [55]. The coating of 540 nm thick CdS film changes the lattice parameters of the AlSb/CdS heterojunctions to a = b = c = 6.46 A^{o}. The increase in the lattice parameter is assigned to the large lattice mismatch between AlSb and CdS. In accordance with equation (2.1), the lattice mismatch $(\Delta) = \frac{|a_{CdS} - a_{AlSb}|}{a_{CdS}}$ is 56.8% along a-axis. The values are extremely high and make the AlSb/CdS heterojunctions suitable for strained electronic device fabrication [56].

Table 4.3 have the grain size (D), microstrain (ε), dislocation density (δ) and stacking faults (SF %) for the substrate and heterojunction are calculated using the previously described Scherrer equation (2.15-2.18). It's clear from these numerical data that the coating of CdS onto AlSb layer caused the strained nature of growth. As the table shows, the insertion of CdS film increased the strain, defect density, stacking faults

and decreased the grain size (D) and in the AlSb/CdS bilayer. This behavior induces high visible light emission intensity [57]. The inclusion of CdS atoms into the structure of AlSb shifted the diffraction angles toward smaller angles, which could be owed to the non-stoichiometric composition. The positions of the vacant of S atoms can be occupied by Cd in portions depending on the film composition [58]. The non-stoichiometric composition causes more defects and vacancies, which lead to the observed poor crystallization process [59].

Table 4.3. The structural parameters of AlSb, CdS and AlSb/CdS films are obtained from the maximum peak FWHM.

Sample	**AlSb**	**CdS**	**AlSb/CdS**
2θ (^{o})	24	26.75	23.85
I (a. u.)	5836	1536	1953
d (A^o)	3.71	3.33	3.73
(hkl)	(1 1 1)	(0 0 2)	(1 1 1)
a (A^o)	6.42	4.10	6.46
b (A^o)	6.42	4.10	6.46
c (A^o)	6.42	6.66	6.46
D (nm)	21	28	15
SF (%)	0.38	0.27	0.53
ε($x10^{-3}$)	8.21	5.51	11.36
δ($x10^{12}$ lines/cm^2)	9.0	7.1	17.1

From a chemical point of view. We consider the interaction between the two layers, assuming the existence of vacancy and/or existence of dangling bonds or weakly reactive bonds. Numerically, the cadmium bond is extremely weak (6.540 A^o) [60], and Cd^{+2} has a tendency to react with any other material. The formation energy of Cd–Cd is small (127.1 kJ/mol) [61], but the bond formation between Cd^{+2} and Al^{+3} or Sb^{+3} is impossible that is due the octet rule obeyed [62,63]. Sulfur has a tendency to react with aluminum. However, the formation energy between S^{-2} and Al^{+3} is high

(381.2 kJ/mol) [64] compared to others. Another possibility is a reaction between sulfur and antimony. The bond length of S-Sb is (2.400 A^o) [65], and the formation of energy is much lower (199.3 kJ/mol) [66] comparable with Cd–S (196.0 kJ/mol) [67]. Also, the Al–Sb bond is weak (2.618 A^o) [68], and the bond energy (216.3 kJ/mol) [69] is larger than that of S–Sb. Such property makes the interaction not preferable, which in turn increased the defect concentrations as observed in this study. The bond lengths and the bonding energies are listed in Table 4.4.

Table 4.4. The bond length and the bond energy of the bonding atoms.

Bond	**Bond length (Å)**	**Bond energy (KJ/mol)**
Cd-Cd	6.540	127.1
Cd-S	2.520	196.0
Cd-Sb	2.910	155.4
Cd-Al	3.300	-
S-S	2.046	226.0
S-AL	2.187	381.2
S-Sb	2.400	191.3
Al-Al	2.450	22.8
Al-Sb	2.618	216.3
Sb-Sb	2.902	176.4

The smaller ionic radius of the heterojunction composers, Sb (76 pm) [70], Al (53 pm) [71] compared to that of Cd (97 pm) [72], S (184 pm) [73] is associated with the lattice deformation and non-chemical interaction, is associated with increased defect density. In addition, the lattice constant increases due to the disordering and lattice distortion which generates internal stresses [74, 75]. One of the reasons, for the increased strain of AlSb/CdS interfaces by 70% is attributed to large lattice mismatches. The large lattice mismatch of heterojunction causes high efficiencies in solar energy conversions. It also may lead to relaxation via the generation of

dislocations [76]. Table 4.5 represents the ionic radius and electronic configuration of the In, Sn, O, Al, Sb, Cd and S atoms.

Table 4.5. The ionic radius and electronic configuration of In, Sn, O, Al, Sb, Cd and S atoms.

Atom	Ionic Radius(pm)	electronic configuration
Cd	97	[Kr] $4d^{10}5s^2$
S	184	[Ne] $3s^2$ $3p^4$
Sb	76	[Kr] $4d^{10}5s^25p^3$
Al	53	[Ne] $3s^2$ 3p1
In	80	[Kr] $4d^{10}$ $5s^2$ $5p^1$
Sn	69	[Kr] $4d^{10}$ $5s^2$ $5p^2$
O	124	[He] $2s^2$ $2p^4$

4.1.4 Structural analysis of ITO/AlSb/CdS

The X-ray diffraction (XRD) patterns of the ITO, ITO/AlSb, ITO/CdS and ITO/AlSb/CdS samples are displayed in Fig. 4.5. As the figure shows, the samples grown onto Indium Tin Oxide (ITO) substrate are found to be of polycrystalline nature. The observed sharp peaks were analyzed with help of "TREOR 92" and "Crystdiff" software packages. The figure has presented that all peaks of the ITO substrates are assigned to cubic structure. The lattice parameters of the cubic phase are a = b = c = 10.12 A°. The other peaks are assigned to the cubic phase of AlSb and hexagonal phase of CdS samples.

Table 4.6 have the grain size (D), microstrain (ε), dislocation density (δ),stacking faults and lattice parameters (SF %) which calculated for the ITO, ITO/AlSb, ITO/CdS and ITO/AlSb/CdS films. The lattice parameters of the observed peaks for the cubic phase of AlSb coated onto the ITO substrate are centered at diffraction angles (2θ) of 24.05^o, 43.90^o and 48.55^o, are calculated by using the equations (2.19)

and found to be a = b = c = 6.41 A°. In addition, the lattice parameters of the observed peaks for the hexagonal phase of CdS coated onto the ITO substrate are centered at diffraction angles (2θ) of 25.90°, 26.80° and 27.55° are calculated by using the equations (2.20), exhibited values of a = b = 4.09, c = 6.65 A°.

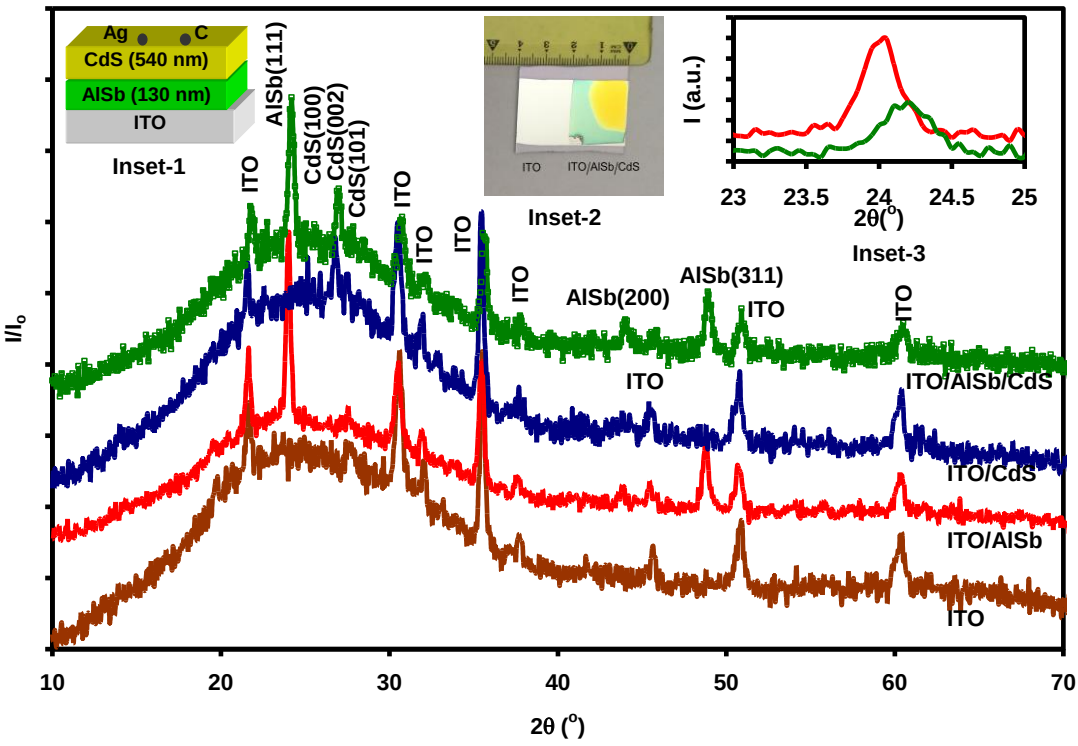

Figure 4.5. The X-ray diffraction patterns for ITO, ITO/AlSb, ITO/CdS and ITO/AlSb/CdS samples. Inset-1 shows the geometrical design of the ITO/AlSb/CdS sample. Inset-2 shows the optical image of the ITO/AlSb/CdS sample. Inset-3 shows the CdS slab effect on the main reflection peak.

The lattice mismatches between the ITO substrates and AlSb layer along a-axis are 57.9%. Particularly, as the bond length of In-O, Sn-O, Al-Sb, In-Sb, Al-O, Sn-Sb are 2.08 A° [77], 2.27 A° [78], 2.618A° [68], 2.93A° [79], 1.74-1.79 A° [80] and 2.8A° [81], respectively, the bonding between the Al and O atoms is much stronger than that of Al and Sb. This property makes the Al atoms have the tendency to move toward oxygen atoms, forcing them to form Al_2O_3 bonds at the interface region between the two materials and induced crystallization take place.

Table 4.6. The structural parameter of ITO/AlSb, ITO/CdS and ITO/AlSb/CdS samples.

Sample	ITO/AlSb	ITO/CdS	ITO/AlSb/CdS
2θ (^{o})	24.05	26.8	24.2
I (a. u.)	1796	1084	1175
d (A^o)	3.70	3.33	3.68
(hkl)	(1 1 1)	(0 0 2)	(1 1 1)
a (A^o)	6.41	4.09	6.37
b (A^o)	6.41	6.65	6.37
c (A^o)	6.41	6.65	6.37
D (nm)	34	34	25
SF (%)	0.24	0.23	0.33
ε(x10^{-3})	5.12	4.58	7.12
δ(x10^{12} lines/cm^2)	3.5	4.9	6.9

4.2 Optical analysis.

4.2.1 The properties of the measured transmittance, reflectance, absorption coefficient.

The effects of coating of CdS thin films on the optical performance of AlSb film are illustrated in Fig. 4.6. The measured transmittance (T) and reflectance (R) spectra of the AlSb, CdS and AlSb/CdS being recorded in the incident photon wavelength (λ) range of 300–1100 nm are shown in Fig. 4.6 (a) and (b), respectively. It is clear from Fig. 4.6 (a) that in the wavelength region of 300–1100 nm, the transmittance of AlSb film decreased with increasing wavelength. While, for CdS film in the wavelength region of 300–560 nm, the transmittance sharply increases with increasing wavelength and then decreases in the range of 560–1100 nm. Such behavior is also observed for AlSb/CdS hetrojunction in the wavelength region of 300–670 nm. The transmittance increases with increasing wavelength till the value of 600 nm is reached. Then it becomes almost invariant.

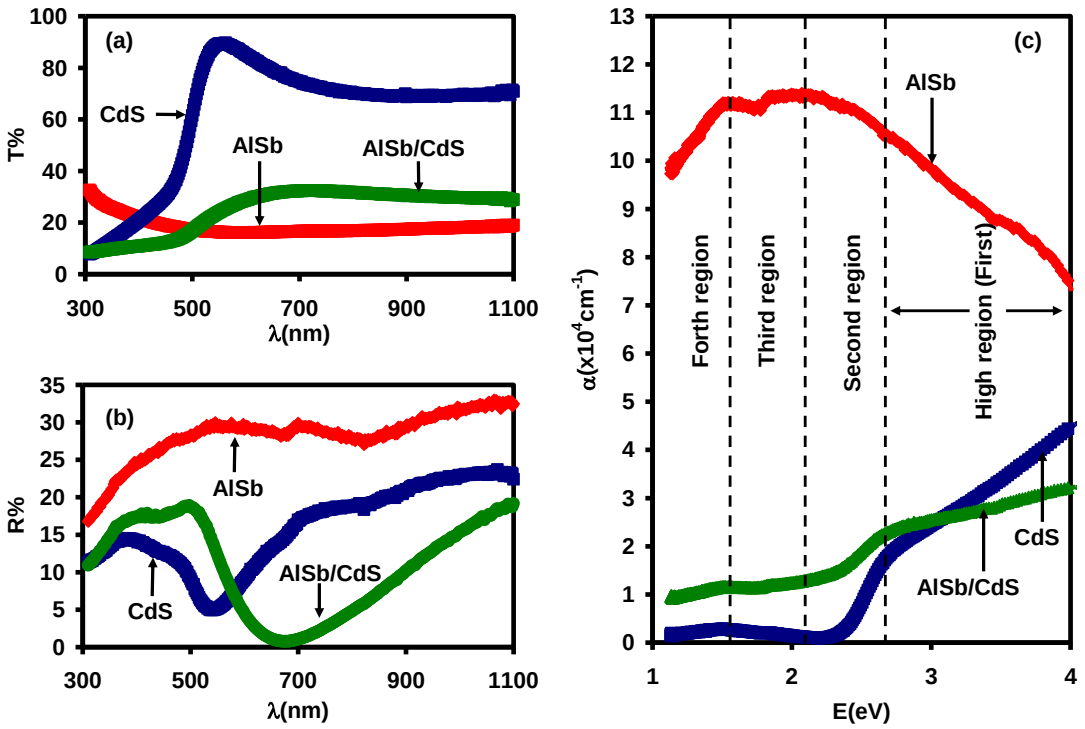

Figure 4.6. (a) The transmittance, (b) the reflectance and (c) the absorption coefficient spectra for the AlSb, CdS and AlSb/CdS films.

On the other hand, the reflectance spectra which are presented in Fig. 4.6 (b) for all samples become effective for incident light wavelengths larger than 370 nm. For all λ < 370 nm, the trend of variation of the AlSb/CdS sample is the same as that of the AlSb layer. It is noticeable that the coating of CdS onto AlSb substrates decreases the values of R of the AlSb/CdS film in the wavelength range of 500 nm to 700 nm. For large λ values it increases. The R spectra of AlSb/CdS show a minor peak at 500 nm (2.5 eV) upon coating of CdS slab onto the layer of AlSb. It is also remarkable from Fig. 4.6 (b) that the reflectance spectra of the AlSb/CdS heterojunction display near zero values in the wavelength region of 660–680 nm. The transmittance of AlSb film is decreasing while the reflectance is increasing with increasing λ is an indication of enhanced surface absorbability of AlSb with increasing λ.

The total effect can be noticed from the absorption coefficient (α) spectra as shown in Fig. 4.6 (c). The α-E spectra, which is determined by the previously described equations (2.30), displays four absorption regions. The high (first) energy region (2.63–4.00 eV) where the α-spectra tends to be saturated due to the generation of carriers resulting in nonlinear renormalization of the band gap with increasing electromagnetic field intensity [17]. As shown from the figure, in the saturated region, a significant effect of the CdS slab is observed. The second region is the sharp absorption region (2.06–2.63 eV). The third region is the low absorption region (1.47–2.06 eV). In this region, a clear redshift can be observed in the α−spectra of CdS deposited on AlSb substrate as compared to those coated onto glass. In the fourth region (1.13–1.47 eV), α−spectra display increasing trends of variation with decreasing incident light energy. Such behavior is generally due to free carrier absorption. The free carrier absorption occurs as a result of the carrier movement that is generated by phonon scattering. The phonon scattering transfers energy to the lattice when irradiated by Infra-Red light [82].

The absorption coefficient spectra of AlSb thin film is presented in Fig. 4.7 (a). As shown from the figure, in contrast to the common behavior of the absorption spectrum of semiconducting material, the α-E spectra of AlSb film decreases with increased incident light energy. This behavior explains the reason for free carrier absorption of a material that has metal like properties. This behavior also may be ascribed to increased permeability within the wavelength (300-1100) nm. It indicates a high probability of electronic transitions [83].

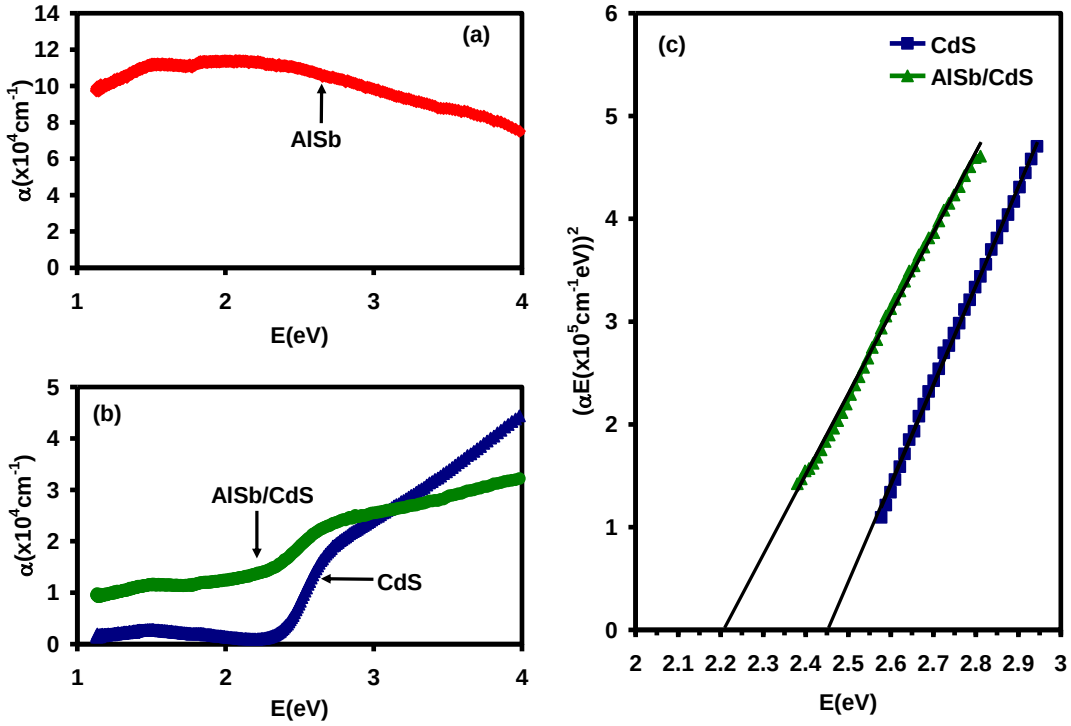

Figure 4.7. (a) the absorption coefficient spectra for the AlSb substrate, (b) the absorption coefficients spectra for the CdS deposited on glass and AlSb substrate films and (c) the Tauc's equation plotting's for the CdS and AlSb/CdS films.

The effects of large lattice mismatches of AlSb/CdS heterojunction on the optical properties are examined from the absorption coefficient (α) spectra which are illustrated in Fig. 4.7 (b). As seen from the figure, the absorption coefficient values of CdS thin films significantly increased upon exchanging the glass substrate by AlSb thin film substrate. Although the $\alpha-$spectra of glass/CdS strongly decreases with decreasing incident photon energy (E) reaching near zero values at 2.17 eV, the $\alpha-$spectra of AlSb/CdS film show a smoother trend of variation and never reach zero but exhibit constant values in the incident photon energy range of 1.13-1.5 eV. The observed nonzero absorption coefficient values in the AlSb, CdS and AlSb/CdS films spectra give evidence about the formation of the interbands and/or band tails in studied materials. That behavior demonstrates the presence of interband transitions followed by band tails effect in the CdS energy band gap. The band tails in the

semiconductor are usually formed by impurities, defects, inhomeganuities and broken bonds in the structure [84]. The existence of interbands in AlSb/CdS hetrojunction is associated with transitions between the defects and different valence states in Cd, S ions (Cd^{+2} and S^{-2}) [56]. Another reason for the presence of interbands contribution could be assigned to the electronic transitions of the bound electrons from filled to the empty bulk band of the material [53].

Fig. 4.7 (c) illustrates the fitting of the Tauc's equation (2.32) for the absorption coefficient spectra in the sharp (second) absorption region. The plotting of $(\alpha E)^2$–E variation was linear only in the region of sharp absorption. The E–axis crossing in that region indicates a remarkable decrease in the energy band gap of CdS deposited onto AlSb thin film substrate. The employment of Tauc equation revealed the direct allowed electronic transitions energy band of values of 2.20 and 2.45 eV for the CdS and AlSb/CdS films, respectively. The direct allowed transitions of the energy band gap of 2.45 eV is consistent with literature data reported for the hexagonal phase of CdS films [85]. Remarkable redshift from 2.20 to 2.45 eV upon coating of CdS is probably due to the lattice mismatches as one reason we have observed in the XRD analysis. Another reason could be the overlapping of atomic orbitals between Cd, Sb, S and Al atoms which form the interbands that lead to the apparent lower gap [86]. The band gap difference is 0.25 eV. Since the electron affinity in n-type CdS is 4.50 eV [87] and that of p-type AlSb is 3.6 eV [88], then the conduction band offset (ΔE_c) for the AlSb/CdS heterojunction device is 0.9 eV. The theoretically expected difference in the energy band gaps ($\Delta Eg = Eg_{AlSb} - Eg_{CdS}$) of AlSb (Eg= 1.6 eV [89]) and CdS is 0.8 eV. The valence band offset (ΔE_v) is 0.1 eV. The differences between the theoretically assumed and the experimentally measured values of energy gap for the heterojunctions could be ascribed to the increased stacking faults, increased defect

density and increased strain (Table 4.3) that arises from the lattice mismatches. These parameters are not considered through theoretical estimations. The redshift in the direct allowed energy band gap upon insertion of CdS film may be attributed to the increase in the lattice parameters, increase in the microstrain and increase in the defect density as we have discussed in the structural analysis. The shrinkage in the band gap of CdS which is observed in this work is assigned to the formation of band tails that probably result from the oxidation process [76]. The interband transitions followed by the band tails is believed to exist in the fourth region.

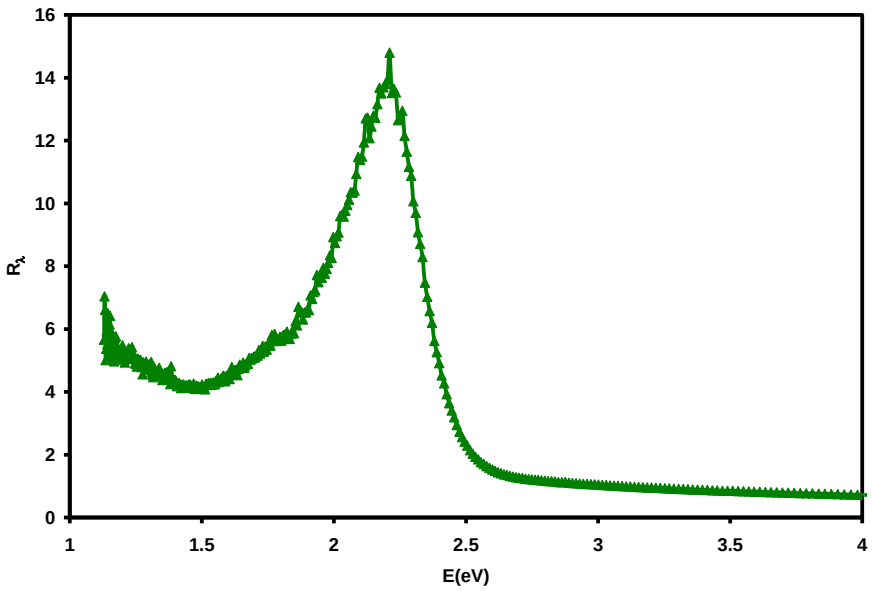

Figure 4.8. The absorbability spectra for the AlSb/CdS heterojunction.

The increase in the ability of the AlSb/CdS to absorb light in the visible light region can be screened from Fig. 4.8.The figure represents the ratio of the absorbance (R_λ) of AlSb/CdS to that of CdS. As it is readable from the figure, the absorbability region of the AlSb/CdS extends from 1.50 to 2.50 eV. It exhibits a maxima in incident light energy of 2.21 eV. The absorbability of light signals reaches 14.79 times for the

heterojunction. Such property makes the heterojunction more appropriate for optoelectronic applications [17]. While the peak which is observed in the R_λ spectra is attributed to the direct allowed electronic transitions near the energy band gap. The enhancement in the light absorbability in this range of visible light spectra is an indication of the success of the large lattice mismatch in enhancing the optical performance of AlSb/CdS film [56].

4.2.2 The properties of the dielectric constant

The width of the energy band tail (E_e) is evaluated from Urbach rule [53], the reciprocal of the linear slope of the plot of ln(α) –*E* variations which is shown in Fig. 4.9 (a). The calculated values of the band tail energy for 540 nm CdS deposited onto glass reveals an energy band tail width of E_e=0.680 eV. Since the electronic configuration of Cd and S are $4d^{10}5s^2$ and $3s^23p^4$ respectively, the Cd atoms with the filled 5s orbitals can easily overlap with the unfilled 3p orbitals of S atoms, leading to the formation of these band tails. This behavior also could be a result of existence vacancy effect in addition to the large number of defects. To test the existence of a band tail for AlSb/CdS, we calculated the width of the energy band tail by using the previous rule and revealed 1.718 eV, compared with the energy band gap of 2.2 eV. The band tail should be within the energy band gap $E_e < \frac{Eg}{2}$. This value suggested that the tails width energy is larger than half of the band gap, which means there is no band tails.

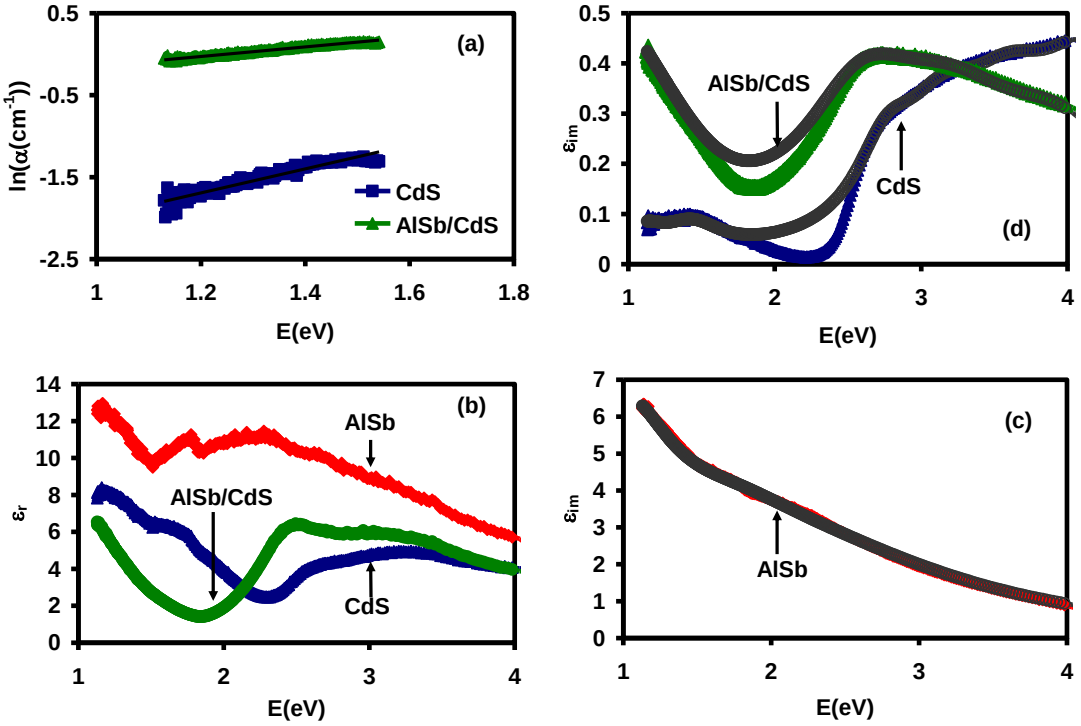

Figure 4.9. (a) The $ln(\alpha)-E$ variations for the CdS and AlSb/CdS films, (b) the real part of the dielectric spectra for the AlSb, CdS and AlSb/CdS films, the imaginary part of the dielectric spectra for (c) AlSb, and (d) CdS and AlSb/CdS films. The dark gray circles in the figure are the fittings that reveal the conduction parameters represented in Table 4.7.

Fig. 4.9 (b), (c) and (d) shows the real (ε_r) and imaginary (ε_{im}) parts of the dielectric constant as determined from the Fresnel's equations. As seen from Fig. 4.9 (b), the dielectric constant values for AlSb film linearly increase with decreasing incident photon energy in the spectral ranges of 1.13–1.50 eV and 2.30–4.00 eV. The increase in the dielectric constant values with decreasing energy provides information about the capacitance spectra. The increase in capacitance values as incident photons approach the infrared region suggests future applications in wireless communications in the terahertz frequency domain [56]. However, the AlSb spectra exhibited two resonance shoulders of dielectric constant values (ε_r) of 11.26 and 11.25 at 1.78 and 2.34 eV, respectively. Namely, while the spectra of 500 nm thick CdS film of our early study [17] exhibited a resonance peak of maximum dielectric constant value

($\varepsilon_{r,\max}$) of 9.13 at 2.27 eV. For our glass/CdS sample, the ε_r spectra displayed no resonance peak but one resonance shoulder of value 4.01 at 2.57 eV. Since the dielectric resonance shoulder appeared at an energy higher than that of the energy band gap, it should be assigned to other reasons. It is noticeable that the real part of the dielectric constant spectra for AlSb/CdS is significantly differing from that of the AlSb substrate. On the other hand, for the AlSb/CdS, the ε_r spectra follow the same trend of variation of glass/CdS and AlSb substrate in the spectral range of 3.2–4.0 eV. For AlSb/CdS double layer there is a redshift in the position of the shoulder of CdS spectra and a rise in the dielectric constant value to 6.27 is detected at 2.45 eV. The shift in the position of the dielectric resonance shoulder upon insertion of CdS could be attributed to the reduction in the recombination rate which is observed to increase the defect density on the surface of CdS films. The filling of sulfur vacancies with donor atoms reduces the recombination rate by forming electron-hole pairs [76]. Another reason for the presence of the dielectric resonance shoulder at 2.45 eV may be the reservation of the sulfur vacant sites by un purposely present oxygen atoms [76]. It is also observable that the dielectric constant values of the double layer exponentially decreases with increasing incident photon energy in the spectral range of 1.13–1.78 eV. This behavior could be assigned to the electronic, ionic and space charge polarizations or may be attributed to the electron–hole recombination due to free carrier absorption near the IR region [57].

It may also be of interest to mention that the high frequency dielectric constant (ε_r^{∞}) values of the AlSb film decreased from 5.72 to 3.96 as a result of the interfacing between the 540 nm CdS on the 130 nm AlSb substrates. The high frequency dielectric constant value (ε (∞)) of CdS deposited on the glass substrate of 3.96 is close to the CdS interfacing with AlSb.

On the other side, the imaginary part of the dielectric spectra which is illustrated in Fig. 4.9 (c) and (d) exhibited lower values for the AlSb/CdS films compared to the AlSb substrate and also achieved higher values compared to the glass/CdS. As seen from Fig. 4.9 (c), ε_{im} of AlSb film follows the same trend of variation from that of the real part but without shoulders. Whereas Fig. 4.9 (d) also presented the same trend of variation for AlSb/CdS heterojunctions and a different one for glass/CdS from the real part that was discussed previously. Particularly, it increases with increasing incident light energy above 2.27 eV for glass/CdS spectra. Moreover, it decreases with increasing incident light energy above 2.64 eV upon glass replacement by AlSb substrate.

The imaginary part of the dielectric constant spectra is modeled according to the Drude-Lorentz model through the modeling relation [90],

$$\varepsilon_{im} = \sum_{i=1}^{k} \frac{w_{pei}^2 \, w}{((w_{ei}^2 - w^2)^2 + w^2 \, \tau_i^{-2})} \tag{4.1}$$

Where, k is the number of dominant linear oscillators, $w_{pe} = \sqrt{4\pi n e^2/m^*}$ is the electron bounded Plasmon frequency, $w = 2\pi f$ is the angular frequency of the incident light, w_e is the reduced resonant frequency, τ is the average scattering time and represents the inverse of the damping coefficient. m^* is the free carrier effective mass and n is the free electron density. The free-carrier mobility is also determined by the formula $\mu = e\tau/m^*$. In this model, substituting the value of the effective mass for holes in AlSb (m^*_{AlSb}) is 0.872 m_o [91] and the electron effective mass in CdS (m^*_{CdS}) is 0.25 m_o [91], then the reduced mass for the AlSb/CdS interfaces is 0.194 m_o. The fitting of the imaginary part equation assuming the presence of six oscillators (k = 6) is shown by dark gray-colored circles in Fig. 4.9 (c) and (d). Good correlation

between the theoretical and experimental spectral data is obtained via the fitting parameters shown in in Fig. 4.9 (c) and (d) which are calculated and tabulated in Table 4.7.

Table 4.7. The optical conduction parameters for AlSb, CdS and AlSb/CdS films.

	AlSb						CdS						AlSb/CdS					
i	1	2	3	4	5	6	1	2	3	4	5	6	1	2	3	4	5	6
τ_i (fs)	1.0	0.6	0.5	0.3	0.3	0.2	2.0	1.3	1.3	0.9	0.8	0.8	1.2	0.8	0.8	0.7	0.5	0.5
n_i ($x10^{18}$ cm^{-3})	98	130	147	240	240	240	0.25	0.6	2.75	6.45	9.1	16.3	1.69	1.8	0.5	7.4	9.5	11
ω_{ei} ($x10^{15}$ Rad/s)	1.6	1.8	2.8	3.65	4	4.5	1.7	2.21	4.2	4.8	5.5	6.3	1.5	1.9	2.2	4	4.95	6.1
ω_{pi} (GHz)	6.3	7.3	7.7	9.9	9.9	9.9	0.6	0.9	2.0	3.0	3.6	4.8	1.8	1.8	1.0	3.7	4.2	4.5
μ_i (cm^2/Vs)	2.0	1.2	1.0	0.5	0.5	0.4	14.1	9.1	9.1	6.3	5.6	5.6	10.9	7.2	7.2	5.9	4.8	4.8

As may be seen from the table, the parameters show that the drift mobility for AlSb deposited onto glass substrates is less than that previously reported for AlSb thin films (400 cm^2/Vs) [92] for the most dominant oscillator (k = 1). The other oscillators (k = 2, …, 6) are of less importance as they are subjected to larger damping coefficients. In addition, the scattering time for CdS deposited onto AlSb substrate decreased, indicating that the damping coefficient increased, leading to more electronic frictional forces [56]. Moreover, the effect of insertion CdS on AlSb substrate raises the free carrier density and reduces the drift mobility. Literature data reported a value of 344 cm^2/Vs for CdS thin films of thickness of 200 nm [76]. The main reason for the varying values of AlSb/CdS might be the large recombination of e-h (holes in AlSb and electrons in CdS). In accordance with Table 4.7, the AlSb substrate changes the range of Plasmon frequency from 6.3–9.9 GHz to 1.8–4.5 GHz. The free carrier density of AlSb is very large showing a metallic character. It can be regarded as hole supplier to the heterojunction device. The higher the oscillation energy is, the larger the free carrier concentration, the larger the plasmon frequency. Since the plasmon frequency provides information about the electromagnetic wave cutoff frequency,

large values of ω_p indicate transitivity of waves below 10 GHz. Such numerical frequency values of AlSb make AlSb suitable for 4G/5G antenna production. The same conclusions can be driven for CdS and AlSb/CdS but with different scales of band filtering.

4.3 Impedance spectroscopy analysis

4.3.1 The measured impedance, reflection coefficient and return loss spectra properties for ITO/AlSb and ITO/AlSb/CdS films.

As a practical application to the proposed ITO/AlSb and ITO/AlSb/CdS devices, the top layer of the device is contacted by carbon (C) circular point contact of an area of 7.14×10^{-3} cm^{-2}. The C is selected owing to its high work function (5.0 eV) [93]. The impedance (Z), reflection coefficient (ρ), return loss (L_r) spectral measurements are carried out in the frequency domain of 10 to 1800 MHz. The impedance spectra for ITO/AlSb and ITO/AlSb/CdS devices is shown in Fig. 4.10 (a). As shown from the figure, while the Z values decreased in the frequency range of 10–150 MHz, that of ITO/AlSb/CdS remains close to the ITO/AlSb in the range of 10–900 MHz. In this frequency range, the impedance spectra of both devices slowly increases with increasing frequency. It then starts decreasing slowly for ITO/AlSb reaching a minimum value at 1420 MHz, and then re-increases with increasing signal frequency, reaching a high impedance value of 58.30 Ω at 1800 MHz. For ITO/AlSb/CdS significantly increased, upon increasing signal frequency in the frequency domain of 900 to 1420 MHz, reaching an impedance value of 68.85 Ω at 1414 MHz, and then sharply decreased, reaching an impedance value of 39.40 Ω at 1500 MHz. After that, the Z spectra again increased, reaching a maximum impedance value of 96.00 Ω at

1630 MHz. It finally re-decreases with increasing frequency in the remaining range of study. The impedance spectra are employed to calculate the magnitude of the reflection coefficient through the relation (2.85).

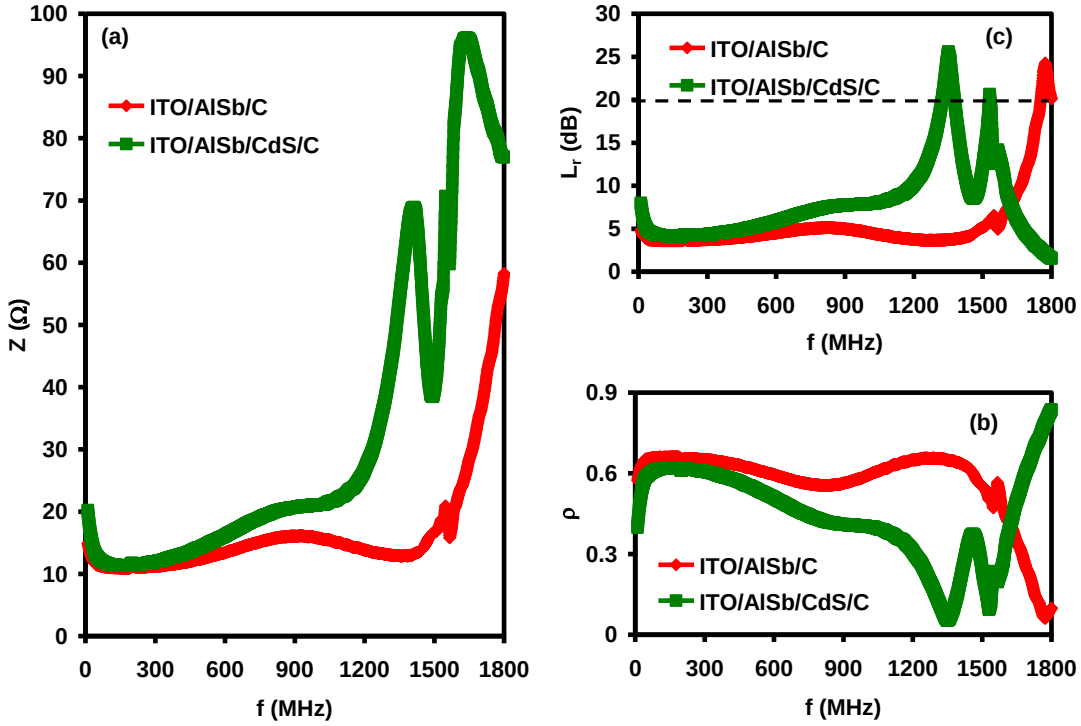

Figure 4.10. (a) The impedance, (b) the magnitude of the reflection coefficient, (c) the return loss spectra for the ITO/AlSb film and ITO/AlSb/CdS heterojunction devices.

The magnitude of the reflection coefficient (ρ) spectra is shown in Fig. 4.10 (b). As appears in Fig. 4.10 (b) below 900 MHz, for both samples, the ρ spectra slightly increases in the frequency domain of 10-120 MHz, and exhibit very low values in the low frequency domain of 120-850 MHz. Above 900 MHz, the ρ spectra display difference behavior between samples after formation of ITO/AlSb/CdS. The device of ITO/AlSb behaves as a low pass filter as ρ approaches zero in the domain of 1300-1800 MHz, where it exhibits ρ values greater than 0.6 in the frequency domain of 1000-1450 MHz. On the other hand, the reflection coefficient spectra for the ITO/AlSb/CdS demonstrates features of double band-stop filters in the domain of

1100-1800 MHz with notch frequencies of 1360 and 1530 MHz. Due to the values of ρ being approaching zero values, and positive, the double band-stop filters are assumed to exhibit a good match between the signal generator (source) and device. The quality of the filtered signals is detected from the return loss (L_r) spectra equation (2.91), which is shown in Fig. 4.10 (c). The acceptable return loss values should exceed 20 dB, if this value is reached then the electromagnetic power transmission between source and device is efficient. While the ITO/AlSb devices return loss spectra reaches a value of 23.97 dB at 1775 MHz. The value of L_r at the notch frequency (1351 MHz) is 25.43 dB for ITO/AlSb/CdS. It may be indicated that the device is ideal for use as a band stop filter.

4.3.2 The measured conductivity and capacitance spectra properties for ITO/AlSb and ITO/AlSb/CdS films.

The transient electrical properties of ITO/AlSb film and the effect of the insertion CdS over ITO/AlSb thin film is evident from the measured conductivity and capacitance spectra in the frequency domain of 10-1800 MHz. The conductivity (σ) spectra for the samples under study are illustrated in Fig. 4.11 (a) and (b). It is clear from Fig. 4.11 (a) that the conductivity of the ITO/AlSb sample sharply increases with increasing AC signal frequency until the frequency reaches a value of 150 MHz. At this value, conductivity exhibits an absolute maximum, then it starts decreasing with increasing frequency until the value of 1090 MHz is reached. After this value, another peak of local maximum appears in the conductivity spectra at the frequency value of 1443 MHz.

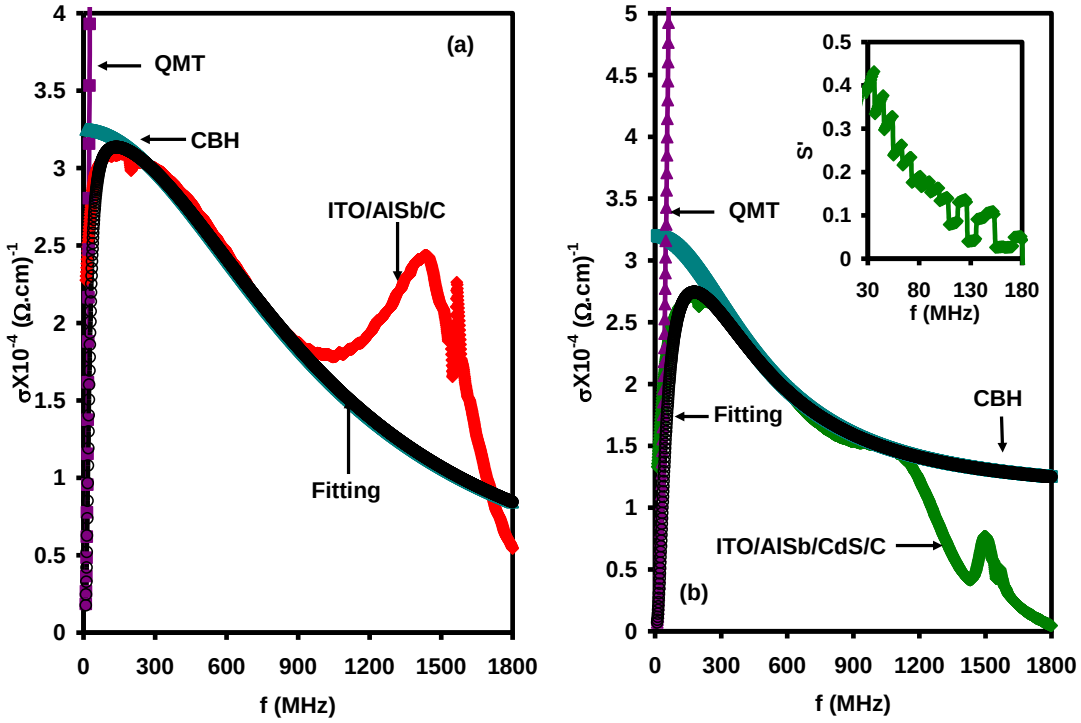

Figure 4.11. (a) and (b) The AC conductivity for ITO/AlSb and ITO/AlSb/CdS films, respectively. The insets of (b) show the S' exponent parameter variation with frequency.

This trend of variations can be explained by assuming the existence of both of the current conductions by quantum mechanical tunneling (QMT) and correlated barrier hopping (CBH) mechanisms [59]. Both of the theoretically estimated σ_{QMT} (w) and σ_{CBH} (w), which are dominant below and above 150 MHz, reaching a frequency value of 900 MHz are shown in Fig. 4.11 (a). The fitting parameters which are calculated by using the equation (2.102) to reproduce the experimental data (black colored circle in Fig. 4.11 (a)) are shown in Table 4.8.

In accordance with the tabulated data, the characteristic relaxation time (τ_o) being 400 fs refers to a phonon frequency value of ν = 83.33 cm^{-1} for the ITO/AlSb device. The density of localized states near the Fermi level is $4x10^{20}$ $cm^{-3}eV^{-1}$. The conductivity in the high frequency range (900−1800 MHz) is also similar in behavior to the low

frequency range and may be achieved by the combined conduction mechanism composed of QMT and CBH mechanisms. Unfortunately, equation (2.102) is not valid for using in this range of frequency (900-1800 MHz), which needed more deep analysis in addition to the existing QMT and CBH.

Table 4.8. The electrical conduction parameters for ITO/AlSb and ITO/AlSb/CdS devices.

parameter	ITO/AlSb/C		ITO/AlSb/CdS/C		
	f < 100 MHz	f > 100 MHz	f < 500 MHz	500 < f < 1000 MHz	f > 1000 MHz
τ_0 (fs)	400.00	400.00	900.00	900.00	900.00
τ_{hop} (ns)	1.00	1.00	2.00	2.00	2.00
ν (cm^{-1})	83.33	83.33	37.04	37.04	37.04
$N(E_F)$ ($x10^{18}$ $cm^{-3}eV$)	400	400	99.9	99.9	99.9
$\sigma(L)$ x (10^{-2} $\Omega^{-1}cm^{-1}$)	0.03	0.03	0.03	0.03	0.03
$\sigma(H)$ x (10^{-6} $\Omega^{-1}cm^{-1}$)	10	10	110	110	110
C_o (pF)	20	9	1000	300	120
a_n	0.2	3.5	4	7	1
a_p	0.1	0.1	2	3	1
w_{pn} (GHz)	0.1	0	1.3	5.2	6.87
w_{pp} (GHz)	0.2	6.3	1.4	5.16	6.89

As seen from Fig. 4.11 (b), the coating of CdS over ITO/AlSb sample follows the same trend of variations of the ITO/AlSb conductivity spectra in the frequency domain of 10-900 MHz, and changed the behavior of the conductivity spectra and decreased its value for all applied frequencies larger than 900 MHz. Particularly, for the ITO/AlSb/CdS/C device, σ-spectra values decreased from 1.33 $(\Omega\ cm)^{-1}$ at 10 MHz to 0.045 $(\Omega\ cm)^{-1}$ when the frequency reaches 1800 MHz. An abnormal minor peak appeared at 1504 MHz. This conductivity behavior was modeled in the heterojunction device assuming domination of quantum mechanical tunneling (QMT) and correlated barriers hopping (CBH) conduction mechanisms. The domination of the tunneling process should be valid as the S parameter decreases with increasing frequency, which is evidenced in the inset of Fig. 4.11 (b). The inset shows that the domination of the quantum tunneling mechanical model is in the range of ~30 MHz to 180 MHz. The good consistency between the experimentally and theoretically

measured AC conductivities in the frequency domain of 10-1140 MHz, which is shown by black colored circles in Fig. 4.11 (b). This solution did not achieve the conductivity values at high frequencies (1140-1800 MHz). This is because the equation assumes the presence of one kind of scattering time in a specific barrier of identical nature that dominates the tunneling and/or hopping. However, our proposed device has two different materials that may form subgap, which could also form another class of correlated barriers. It means some further work must be attempted to reach two featured solutions above and below 1140 MHz. The fitting parameters of the ITO/AlSb/CdS device are shown in Table 4.8. According to the data of Table 4.8, the insertion of the CdS layer achieved relaxation time (τ_o) of 0.9 ps refers to a phonon frequency value of ν = 37.04 cm^{-1}. The density of states near the fermi level is $1.00x10^{20}$ $cm^{-3}eV^{-1}$. In addition, the increasing values of the σ_{AC} (H) and constant values of σ_{AC} (L) can be due to the orbital energy bands overlapping [94]. Moreover, the increase in the relaxation time is ascribed to the structural modifications [94]. In accordance with our X-ray analysis, the insertion of a semiconducting material that causes reduction in the grains sizes and increased values of the defect density and stacking faults also means larger probability of charge carrier hoping. We believe that upon interfacing of CdS with AlSb film, the large defect density which acts as trap centers can prevent control of resistivity through doping or field effect [95].

On the other hand, the capacitance spectra of the ITO/AlSb/C and ITO/AlSb/CdS/C samples are illustrated in Fig. 4.12 (a) and (b), respectively. Although, the C-spectra of the ITO/AlSb/C sample showed a decreasing trend of variation with increasing signal frequency, it displayed one resonance peak at 17 MHz. Reproduction of using equation (2.123) experimental data of the ITO/AlSb capacitance spectra, which reveal

the black circles in Fig. 4.12 (a) with the tabulated values of the computed parameters (a_n, a_p, w_n, w_p) are shown in Table 4.8.

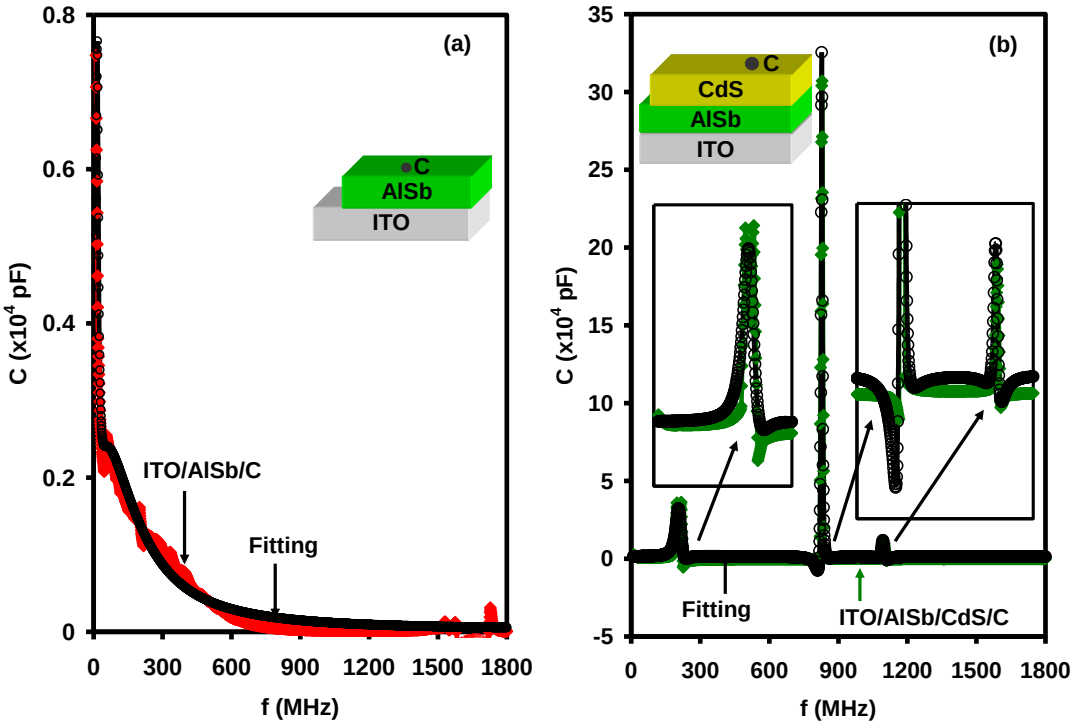

Figure 4.12. (a) and (b) The capacitance spectra for ITO/AlSb and ITO/AlSb/CdS Schottky barriers, respectively. The insets of (a) and (b) show the geometrical design of the measured samples.

The ITO/AlSb/CdS/C device displays strong resonance peaks centered at 217 MHz, 829 MHz and at 1098 MHz followed by a weak antiresonance phenomena appeared at 226 MHz, 819 MHz and at 1108 MHz, respectively. The resonance peaks in Fig. 4.12 (b) gain importance as they indicate storability of electromagnetic energy at these critical frequency values [48]. While the resonance occurs at positive capacitance values, antiresonance appears in the negative range of capacitance. In the remaining frequency domain of 1160–1800 MHz, the capacitance spectra remain positive. The Qasrawi–Ershov approach for AC conduction is employed to understand the experimental data of the capacitance spectra for the device under study. Reproduction of the experimental data of the capacitance spectra shown by black circles in Fig. 4.12

(b), which was achieved by equation (2.123), assuming the fitting parameters shown in Table 4.8. Because of their negative capacitance effect in the microwave frequency domain, heterojunctions are beneficial for parasitic capacitance cancellations and noise reduction [96].

4.3.3 The measured impedance, resistance, reflection coefficient and return loss spectra properties for AlSb bulk device.

Fig. 4.13 (a) shows the resulting impedance (Z) spectra for the AlSb bulk device. As evident from this figure, the impedance spectra show a weak decreasing trend of variation in the frequency range of 10–300 MHz. It then starts slightly increasing with increasing frequency, with an abnormal maximum appearing at a frequency value of 1200 MHz. The Z spectra then significantly increased with increasing frequency, reaching a high impedance value of 94.26 Ω at 1800 MHz. Such behavior is shown in the ITO/AlSb thin film that was previously reported. The resistance which is shown in the Fig. 4.13 (b), decreases with increasing frequency values, reaching a resistance value of -50.7Ω at 1800 MHz. It interests to mention that, the resistance of the bulk being negative above a frequency value of 1525 MHz. The negative resistance means there are n-stable and p-stable charges in the bulk alloy. Negative resistance suggests useful future applications in microwave resonators [97].

The impedance spectra are used to calculate the magnitude of the reflection coefficient through the relation (2.90). The magnitude of the reflection coefficient (ρ) spectra is shown in Fig. 4.13 (c). The ρ values increase with increasing frequency, reaching a value of 1.61 at 1800 MHz. This property is characteristic of high pass filters. Due to the values of ρ being larger than one and positive, the high-pass filters

are supposed to reject all incident waves. The quality of this filter is characterized from the return loss (L_r) values which are shown in Fig. 4.13 (d). A good match always requires L_r values greater than 20 dB. For our proposed device, the value of L_r at the notch frequency (1800 MHz) is -4.16 dB. A clear difference in the performance is observed between Al_xSb_y thin film and Al_xSb_y bulk form in the last two figures.

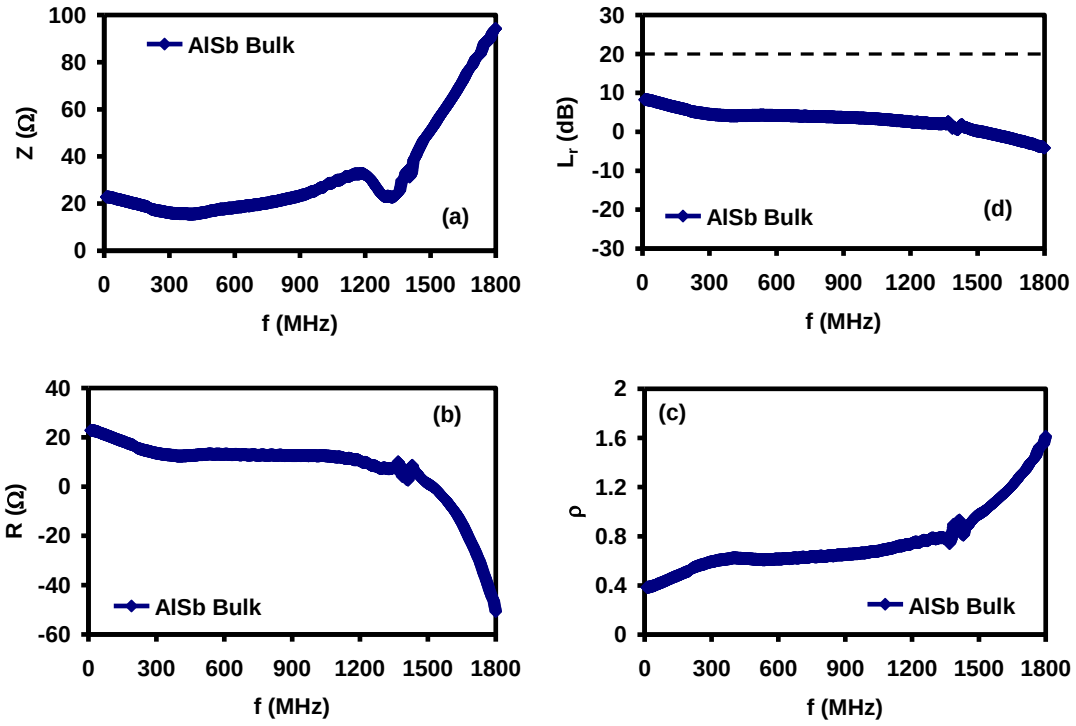

Figure 4.13 (a) The impedance, (b) the resistance, (c) the magnitude of the reflection coefficient, (d) the return loss spectra for the AlSb bulk devices.

4.3.4 The measured conductance and capacitance spectra properties for AlSb bulk device.

Fig. 4.14 (a) and (b) illustrates the conductance (G) and capacitance (C) spectra being recorded in the frequency domain of 10–1800 MHz. In accordance with Fig.4.14 (a), the conductance spectra of AlSb bulk slightly increases with increasing frequency up to 355 MHz, then starts sharply

decrease with increasing signal frequency, with an abnormal peak appearing at a frequency value of 1320 MHz. In general, the slope of variation of the G-f curve is positive and negative below and above 355 MHz, respectively. This dynamical behavior of the conductance is due to the domination of quantum mechanical tunneling of charged particles below 355 MHz and ascribed to the domination of the correlated barrier hopping conduction mechanism above 355 MHz. In addition, negative conductance could be causing the negative resistance phenomenon which we mentioned above. On the other hand, the capacitance spectra for the AlSb bulk device, which is illustrated in Fig. 4.14 (b), show positive capacitance effect in all the studied frequency domain. It exhibits a very narrow peak at 10 MHz. Also, we observed that the features of the bulk device are not much different from those previously obtained by ITO/AlSb thin film device.

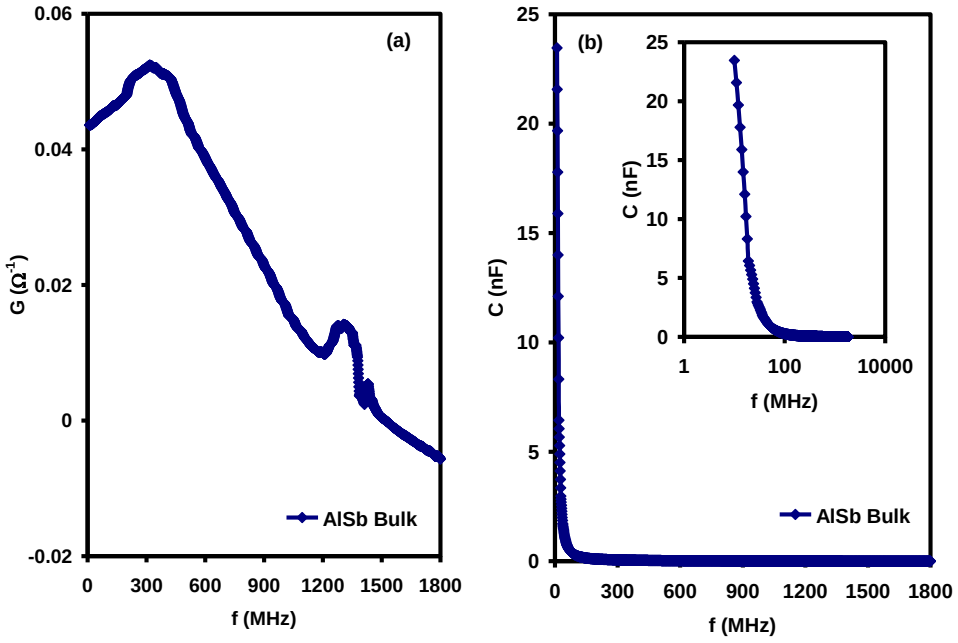

Figure 4.14. (a) The conductance and (b) the capacitance spectra for AlSb bulk devices.

Chapter 5

Conclusions

In this thesis, we studied the basic physical properties of AlSb in the bulk and thin film forms. The films which are prepared as substrates to form AlSb/CdS heterojunction devices were grown by the thermal evaporation technique at sufficiently high vacuum pressure. Investigation on these films were carried out by the X-ray diffraction (XRD), ultraviolet-visible light spectrophotometry, impedance spectroscopy and direct current analysis. In addition to the experimental investigations, while the XRD results were analyzed by the "TREOR 92" and "Crystdiff" software packages, the optical data and impedance spectroscopy were theoretically studied by the Drude-Lorentz and Ershov-Qasrawi models. The XRD analyses have shown that formation of hexagonal CdS onto cubic AlSb substrates result in highly strained structure associated with large lattice mismatches. These two parameters are the keys which control the optical and electrical properties of the AlSb/CdS heterojunctions. Optically, well aligned valance bands with band offset of 0.1 eV are achieved. The conduction band offset is 0.90 eV. It is also concluded that stacking of AlSb with CdS enhances the light absorbability of CdS by more than 14 times in the visible range of light. From dielectric point of view, stacking of the two layers increased the free carrier density, shifted the main IR oscillator energy and changed operative range of plasmon frequency from radiowave to microwave ranges. On the other hand, the impedance spectroscopy analyses have shown the ability of employing the stacked layers of AlSb and CdS as microwave resonators and band filters. The heterojunctions are also beneficial for parasitic capacitance cancellations and noise reduction as they exhibit negative capacitance effect in the microwave frequency domain. The return loss values of the heterojunctions when used as high

pass filters are comparable with the commercially produced ones indicating the suitability of these thin film band as filters for use in 4G/5G technologies.

We believe that further work must be done to reduce the metallic character of AlSb substrates to make them on standing in optoelectronic technologies. Thus, it is one of our future works to find alternative method for producing AlSb thin films of nondegenerate semiconductor characteristics rather than metallic type. We also target studying other photosensitive heterojunctions formed onto AlSb after reaching the requested enhancements.

References

[1] Nguyen, X. A., Kim, T. J., Le, V. L., Park, H. G., Nguyen, H. T., & Kim, Y. D. (2019). A Parametric Model for Temperature Dependence of Dielectric Function of AlSb Film. Journal of nanoscience and nanotechnology, 19(10), 6801-6807.

[2] Yin, Z., Jie, W., Zhang, X., & Wang, T. (2020). Adhesion-free Bridgman growth of AlSb. Journal of Crystal Growth, 125641.

[3] Athab, R. H., Hussein, B. H., & Makki, S. A. (2019, July). Effect of in on the properties of AlSb thin film solar cell. In AIP Conference Proceedings (Vol. 2123, No. 1, p. 020030). AIP Publishing LLC.

[4] Tang, P., Wang, W., Li, B., Feng, L., & Zeng, G. (2019). The Properties of Zn-Doped AlSb Thin Films Prepared by Pulsed Laser Deposition. Coatings, 9(2), 136.

[5] Li, M., Li, B., Zeng, G., & Song, H. (2021). Preparation of AlSb thin films on stainless steel flexible substrates and preventive measures of its deliquescence. Materials Science in Semiconductor Processing, 121, 105410.

[6] Dey, M., Chakma, R., Dey, M., & Das, N. K. (2019, February). Optimization of AlSb Solar Cell to Improve PCE. In 2019 International Conference on Electrical, Computer and Communication Engineering (ECCE) (pp. 1-5). IEEE.

[7] Xiao, R., Pei, Y., Yan, H., Li, B., Yang, K., Liu, J., & Liu, X. (2019). Phase formation process of AlSb thick films prepared by screen printing and sintering method. Materials Science in Semiconductor Processing, 100, 56-60.

[8] Ali, M. A., Aleem, H., Sarwar, B., & Murtaza, G. (2020). First-principles calculations for optoelectronic properties of AlSb and GaSb under influence of spin–orbit interaction effect. Indian Journal of Physics, 94(4), 477-484.

[9] Haberecht HRR, Middleton AE. Preparation and properties of aluminum antimonide. J Electrochem Soc 1958;105:533–540.

[10] Udofia, B. E. (2019). Substitutional and vacancy defects in two-dimensional AlSb: A first principle approach (Doctoral dissertation).

[11] Yin, Z., Jie, W., Zhang, X., & Wang, T. (2020). The effect of Te dopant on the optical and electrical properties of high-resistivity AlSb crystals. Journal of Applied Physics, 128(2), 025702.

[12] Shawon, A. K. M., & Ur, S. C. (2019). Mechanical and thermoelectric properties of bulk AlSb synthesized by controlled melting, pulverizing and subsequent vacuum hot pressing. Applied Sciences, 9(8), 1609.

[13] Shawon, A. A., Kim, I. H., & Ur, S. C. (2020). Composite fabrication for improvement of thermoelectric properties in AlSb. Materials Science in Semiconductor Processing, 110, 104974.

[14] Salmi, L., Meradji, H., Ghemid, S., Nemiri, O., Oumelaz, F., & Khenata, R. (2020). Phase stability, pressure-induced phase transition and electronic properties of AlX (X= P, As and Sb) compounds from first principle calculations. Phase Transitions, 1-13.

[15] Li, J. Y., Li, Y. H., Qi, M. Y., Lin, Q., Tang, Z. R., & Xu, Y. J. (2020). Selective Organic Transformations over Cadmium Sulfide-Based Photocatalysts. ACS Catalysis.

[16] Kareem, M. M., Mezher, S. J., & Beddai, A. A. (2019). Single crystal cadmium sulfide thin films prepared by thermal evaporation technique. Journal of Non-Oxide Glasses Vol, 11(2), 27-31.

[17] Qasrawi, A. F., & Abed, T. Y. (2019). Structural and optoelectronic properties of CdS/Y/CdS thin films. Thin Solid Films, 679, 72-78.

[18] Zhu, Y. C., Xu, Y. T., Xue, Y., Fan, G. C., Zhang, P. K., Zhao, W. W., ... & Chen, H. Y. (2019). Three-dimensional CdS@ carbon fiber networks: innovative synthesis and application as a general platform for photoelectrochemical bioanalysis. Analytical chemistry, 91(10), 6419-6423.

[19] Feng, C., Chen, Z., Jing, J., Sun, M., Tian, J., Han, J., ... & Ma, L. (2020). Synthesis of a novel three-dimensional sponge-like microporous CdS film with high photoelectrochemical performance and stability. Journal of Electroanalytical Chemistry, 874, 114524.

[20] Zhong, W., Shen, S., He, M., Wang, D., Wang, Z., Lin, Z., ... & Yu, J. (2019). The pulsed laser-induced Schottky junction via in-situ forming Cd clusters on CdS surfaces toward efficient visible light-driven photocatalytic hydrogen evolution. Applied Catalysis B: Environmental, 258, 117967.

[21] Ge, B., Ren, G., Zhao, P., Jin, C., Li, W., & Zhang, Z. (2019). Preparation of superhydrophobic CdS cotton using visible light response and its application for the control of water pollution. Science China Technological Sciences, 62(12), 2236-2242.

[22] Nivetha, A., Devi, S. M., & Prabha, I. (2019). Fascinating Physic-Chemical Properties and Resourceful Applications of Selected Cadmium Nanomaterials. Journal of Inorganic and Organometallic Polymers and Materials, 29(5), 1423-1438.

[23] Majumder, S., Mendhe, A. C., & Sankapal, B. R. (2019). Nanoheterojunction through PbS nanoparticles anchored CdS nanowires towards solar cell application. International Journal of Hydrogen Energy, 44(14), 7095-7107.

[24] Dhatchinamurthy, L., Thirumoorthy, P., Arunraja, L., & Karthikeyan, S. (2020). Synthesis and characterization of cadmium sulfide (CdS) thin film for solar cell applications grown by dip coating method. Materials Today: Proceedings, 26, 3595-3599.

[25] Nadarajah, M., Gour, K. S., & Singh, V. N. (2020). Sputtered Cadmium Sulfide (CdS) Buffer Layer for Kesterite and Chalcogenide Thin Film Solar Cell (TFSC) Applications. Journal of Nanoscience and Nanotechnology, 20(6), 3909-3912.

[26] Perez-Donoso, J. M., Órdenes-Aenishanslins, N., Anziani-Ostuni, G., Quezada, C. P., Rodrigo, E. G., & Denisse, B. (2019). Biological synthesis of CdS/CdSe core/shell nanoparticles and its application in quantum dot sensitized solar cells. Frontiers in microbiology, 10, 1587.

[27] Yin, H. (2020). Mechanism and Applications of large and persistent photoconductivity in cadmium sulfide (Doctoral dissertation, Massachusetts Institute of Technology).

[28] Anand, S. K., Sivasankaran, U., Jose, A. R., & Kumar, K. G. (2019). Interaction of tetracycline with l-cysteine functionalized CdS quantum dots-Fundamentals and sensing application. Spectrochimica Acta Part A: Molecular and Biomolecular Spectroscopy, 213, 410-415.

[29] Oloore, L. E., Gondal, M. A., Popoola, I. K., & Popoola, A. (2020). Cadmium Sulfide Quantum Dots–Organometallic Halide Perovskite Bilayer Electrode Structures for Supercapacitor Applications. ChemElectroChem, 7(2), 486-492.

[30] AlFaify, S., Haritha, L., Manthrammel, M. A., Ganesh, V., Chandekar, K. V., Shaikh, S. S., & Shkir, M. (2020). Fabrication and characterization of Sn: CdS films for optical-nonlinear-limiting applications. Optics & Laser Technology, 126, 106122.

[31] Pei, Y., Yan, H., Xiao, R., Li, B., Yang, K., & Song, H. (2020). Structural, optical, electrical and deliquescent properties of AlSb: Cu thin films prepared by magnetron sputtering. Vacuum, 109341.

[32] Xiao, R., Yan, H., Pei, Y., Li, B., Yang, K., Liu, J., & Liu, X. (2019). Preparation of AlSb film by screen printing and sintering method. Journal of Materials Science: Materials in Electronics, 30(14), 13290-13296.

[33] Rajaram, P. (2019). Single Step Electrode position of AlSb Thin Films. Materials Today: Proceedings, 16, 636-639.

[34] Shkir, M., Ashraf, I. M., AlFaify, S., El-Toni, A. M., Ahmed, M., & Khan, A. (2020). A noticeable effect of Pr doping on key optoelectrical properties of CdS thin films prepared using spray pyrolysis technique for high-performance photodetector applications. Ceramics International, 46(4), 4652-4663.

[35] S. M. Sze and K. K. Ng, Physics of Semiconductor Devices (John Wiley & Sons, N.Y., 2007).

[36] ORTATATLI, Ş. (2013). The crystal structure analysis of a dinuclear Rh (1) n-heterocyclic carbene complex (Doctoral dissertation, DEÜ Fen Bilimleri Enstitüsü).

[37] Kittel, C., McEuen, P., & McEuen, P. (1996). Introduction to solid state physics (Vol. 8, pp. 105-130). New York: Wiley.

[38] Klug, H. P., & Alexander, L. E. (1974). X-ray diffraction procedures: for polycrystalline and amorphous materials (p. 992).

[39] Priya, R., Raman, M. S., Kumar, N. S., Chandrasekaran, J., & Balan, R. (2016). Synthesis and characterization of CTAB-assisted WO_3 deposited on silicon for the fabrication of photoresponse pn junction diode. Optik, 127(19), 7913-7924.

[40] S. R.Alharbi & A. F. Qasrawi (2018). Gold and ytterbium interfacing effects on the properties of the CdSe/Yb/CdSe nanosandwiched structures. Current Applied Physics, 18(8), 946-951.

[41] Omar, A., Qasrawi, A. F., & Gasanly, N. M. (2017). Temperature effects on the structural and optical properties of the TlInSe2xS2 (1− x) mixed crystals (x= 0.3). Journal of Alloys and Compounds, 724, 98-102.

[42] Jeffrey, P. (2016). X-ray Data Collection Course, v0. 6.

[43] Kulawiak, M., & Chybicki, A. (2018). Application of Web-GIS and geovisual analytics to monitoring of seabed evolution in South Baltic Sea coastal areas. Marine Geodesy, 41(4), 405-426.

[44] Fox, M. (2002). Optical properties of solids.

[45] Wager, J. F. (2017). Real-and reciprocal-space attributes of band tail states. AIP Advances, 7(12), 125321.

[46] Aslam, M., Kalyar, M. A., & Raza, Z. A. (2017). Graphene oxides nanosheets mediation of poly (vinyl alcohol) films in tuning their structural and opto-mechanical attributes. Journal of Materials Science: Materials in Electronics, 28(18), 13401-13413.

[47] Attwood, David (1999). Soft X-rays and extreme ultraviolet radiation: principles and applications. p. 60. ISBN 978-0-521-02997-1.

[48] Qasrawi, A. F., & Khanfar, H. K. (2020). Al/MoO 3/ZnPc/Al Broken Gap Tunneling Hybrid Devices Design for IR Laser Sensing and Microwave Filtering. IEEE Sensors Journal, 20(24), 14772-14779.

[49] Ghosh, A. (1990). Frequency-dependent conductivity in bismuth-vanadate glassy semiconductors. Physical review B, 41(3), 1479.

[50] Shim, J., Kang, D. H., Kim, Y., Kum, H., Kong, W., Bae, S. H., … & Kim, J. (2018). Recent progress in Van der Waals (vdW) heterojunction-based electronic and optoelectronic devices. Carbon, 133, 78-89.

[51] Polonsky, A. T., Echlin, M. P., Lenthe, W. C., Dehoff, R. R., Kirka, M. M., & Pollock, T. M. (2018). Defects and 3D structural inhomogeneity in electron beam additively manufactured Inconel 718. Materials Characterization, 143, 171-181.

[52] Hasan, B. A., & Uamran, D. A. (2019, July). Effect of aluminum content on the structural, morphology, and electrical properties of Al1-x Sbx thin films. In Journal of Physics: Conference Series (Vol. 1234, No. 1, p. 012044). IOP Publishing.

[53] Al Garni, S. E., & Qasrawi, A. F. (2019). Design and characterization of MoO3/CdSe heterojunctions. Physica E: Low-dimensional Systems and Nanostructures, 105, 162-167.

[54] Qasrawi, A. F., & Zyoud, H. M. (2020). Dielectric dispersion at the Mn/ZnPc interfaces. physica status solidi (b), 257(6), 2000089.

[55] Jung, G. J., Lee, Y., Mun, Y. S., Kim, H., Hur, J., Kim, T. Y., ... & Kim, I. T. (2017). Sb-AlC0. 75-C composite anodes for high-performance sodium-ion batteries. Journal of Power Sources, 340, 393-400.

[56] Al Garni, S. E., & Qasrawi, A. F. (2018). Characterization of Bi2O3/ZnS heterojunctions designed for visible light communications. Materials Research Express, 6(3), 036205.

[57] Qasrawi, A. F., & Omareya, O. A. (2019). Formation and Characterization of Cd 2 S 3 Polycrystalline Films onto Glass and Lanthanum Substrates. Journal of Electronic Materials, 48(4), 2350-2355.

[58] Qasrawi, A. F., & Shehada, S. R. (2018). Dielectric dispersion in InSe/CdS bilayers. Physica E: Low-dimensional Systems and Nanostructures, 103, 151-155.

[59] Qasrawi, A. F. (2020). Characterization of Au/As2Se3 Multifunctional Tunneling Devices. physica status solidi (a), 217(5), 1900899.

[60] Han, A., Su, H., Xu, G., Khan, M. A., & Li, H. (2020). Synthesis, crystal structures, and luminescent properties of Zn (ii), Cd (ii), Eu (iii) complexes and detection of Fe (iii) ions based on a diacylhydrazone Schiff base. RSC Advances, 10(39), 23372-23378.

[61] Hegab, N. A., Farid, A. S., Shakra, A. M., Afifi, M. A., & Alrebati, A. M. (2016). Compositional Dependence of the Optical Properties of Amorphous Semiconducting Glass Se 80 Ge 20− x Cd x (0≤ x≤ 12 at.%) Thin Films. Journal of Electronic Materials, 45(7), 3332-3339.

[62] Santamaria-Perez, D., & Liebau, F. (2010). Structural relationships between intermetallic clathrates, porous tectosilicates and clathrate hydrates. Inorganic 3D Structures, 1-29.

[63] Akiba, K. Y. (2011). Organo Main Group Chemistry. John Wiley & Sons.

[64] Guha, S., & Francisco, J. S. (2007). An Ab Initio Study of the Structures, Vibrational Spectra, and Energetics of AlSHX (X=–1, 0,+ 1). The Astrophysical Journal, 671(2), 2159.

[65] Yang, H., Li, M., Fu, L., Tang, A., & Mann, S. (2013). Controlled assembly of Sb 2 S 3 nanoparticles on silica/polymer nanotubes: insights into the nature of hybrid interfaces. Scientific reports, 3, 1336.

[66] Boukhris, I., & Kebaili, I. (2021). The effect of adding CsCl content on physicochemical properties of (GeS2–Sb2S3) 100-x (CsCl) x (0≤ x≤ 40 mol%) chalcohalide glasses.

[67] Li, K., Chen, C., Lu, S., Wang, C., Wang, S., Lu, Y., & Tang, J. (2019). Orientation engineering in low-dimensional crystal-structural materials via seed screening. Advanced Materials, 31(44), 1903914.

[68] Zhang, Y. X., Shi, S. P., Liu, Y. L., Yan, M., Zhao, X. F., & Jiang, G. (2018). Structural and electronic properties of SbnAl (0,±1)(n= 1–10) clusters using density-functional theory. Chinese Journal of Physics, 56(4), 1743-1755.

[69] Ramesh, K. (2017). Electrical switching in Sb doped Al23Te77 glasses. Journal of Physics and Chemistry of Solids, 107, 68-74.

[70] Hu, G., Shi, Y., Fan, J., Cao, Y., Peng, Z., Zhang, Y., ... & Du, K. (2020). Sb doping and Sb2O3 coating collaboration to improve the electrochemical performance of LiNi0. 5Mn0. 5O2 cathode material for lithium ion batteries. Electrochimica Acta, 137127.

[71] Kızılaslan, A., Kırkbınar, M., Cetinkaya, T., & Akbulut, H. (2020). Sulfur doped Li 1.3 Al 0.3 Ti 1.7 (PO 4) 3 solid electrolytes with enhanced ionic conductivity and a reduced activation energy barrier. Physical Chemistry Chemical Physics, 22(30), 17221-17228.

[72] Saxena, P., Choudhary, P., Yadav, A., Dewangan, B., Rai, V. N., & Mishra, A. (2020). Improved structural and dielectric properties of Cd and Ti dual doped ZnO nanoparticles. Applied Physics A, 126(10), 1-11.

[73] Song, S., Yan, Z., Wu, F., Zhang, X., & Xiang, Y. (2020). Electrochemical stability and ionic conductivity of solid electrolytes based on Li 10 GeP 2 S 12-x A x (A= O, Se. x= 0, 0.2, 0.4, 0.6, 0.8, 1). E&ES, 461(1), 012074.

[74] Portnoi, V. K., Leonov, A. V., Fadeeva, V. I., & Fedotov, S. A. (2007). Mechanochemical synthesis in the Ni-Al-C system. Bulletin of the Russian Academy of Sciences: Physics, 71(12), 1693-1696.

[75] Hemeda, O. M., Said, M. Z., & Barakat, M. M. (2001). Spectral and transport phenomena in Ni ferrite-substituted Gd2O3. Journal of magnetism and magnetic materials, 224(2), 132-142.

[76] Abed, T. Y., Qasrawi, A. F., & Al Garni, S. E. (2018). Investigation of the physical properties of the Yb nanosandwiched CdS films. Journal of Alloys and Compounds, 731, 1022-1028.

[77] Al Garni, S. E., & Qasrawi, A. F. (2019). Exploring the optical dynamics in the ITO/As 2 Se 3 interfaces. Journal of Electronic Materials, 48(10), 6319-6326.

[78] Yao, Y., Li, Z., Wang, T., Lu, K., Zhang, P., Zhang, W., & Yin, J. (2019). Density functional theory insight towards high sensitivity for NO, NO2 and O2 over monolayer SnO. Materials Research Express, 6(9), 095078.

[79] Foos, E. E., Wells, R. L., & Rheingold, A. L. (1999). Preparation of Nanocrystalline Indium Antimonide Through β-Hydride Elimination from New Indium-Antimony Single-Source Precursors. Journal of Cluster Science, 10(1), 121-131.

[80] Park, J. H., Min, D. J., & Song, H. S. (2002). Structural investigation of CaO–Al2O3 and CaO–Al2O3–CaF2 slags via Fourier transform infrared spectra. ISIJ international, 42(1), 38-43.

[81] Zhang, L., Du, M. H., & Singh, D. J. (2010). Zintl-phase compounds with SnSb 4 tetrahedral anions: Electronic structure and thermoelectric properties. Physical Review B, 81(7), 075117.

[82] Lai, J., Zhang, J., Mao, Y., Lin, L., Min, J., Liang, X., ... & Wang, L. (2018). Distribution of Te inclusions in CdMnTe crystal grown by traveling heater method. Journal of Electronic Materials, 47(8), 4219-4225.

[83] Shakir, W. A., Abdullah, S. H., Mustafa, F. I., Ateia, K. K., & Ibraheem, A. M. Optical properties of (ZnTiO3)/Epoxy Nanocomposite Thin films.

[84] Qasrawi, A. F. (2019). Effect of Y, Au and YAu Nanosandwiching on the structural, optical and dielectric properties of ZnSe thin films.

[85] Rahman, M. F., Hossain, J., Kuddus, A., Tabassum, S., Rubel, M. H., Shirai, H., & Ismail, A. B. M. (2020). A novel synthesis and characterization of transparent CdS thin films for CdTe/CdS solar cells. Applied Physics A, 126(2), 1-11.

[86] Khusayfan, N. M., & Khanfar, H. K. (2018). Characterization of CdS/Sb2Te3 micro/nano-interfaces. Optik, 158, 1154-1159.

[87] Han, F., Meng, G., Zhao, X., Xu, Q., Liu, J., Chen, B., ... & Kong, M. (2009). Building desired heterojunctions of semiconductor CdS nanowire and carbon nanotube via AAO template-based approach. Materials Letters, 63(26), 2249-2252.

[88] Tang, P., Li, B., Feng, L., Wu, L., Zhang, J., Li, W., ... & Liu, C. (2017). Structural, electrical and optical properties of AlSb thin films deposited by pulsed laser deposition. Journal of Alloys and Compounds, 692, 22-25.

[89] Bouarissa, N., Algarni, H., & Khan, M. A. (2020). Positron chemical potential and diffusion constant in AlSb crystal compound under compression. Journal of Electron Spectroscopy and Related Phenomena, 245, 147010.

[90] Kayed, T. S., & Qasrawi, A. F. (2020). Pseudodielectric Dispersion in As2Se3 Thin Films. physica status solidi (b), 257(3), 1900548.

[91] Madelung, O. (Ed.). (2012). Semiconductors: group IV elements and III-V compounds. Springer Science & Business Media.

[92] Cheng, K. A., Yang, C. H., & Yang, M. J. (2000). Nanometer-size InAs/AlSb quantum wires: Fabrication and characterization of Aharonov–Bohm quantum rings. Journal of Applied Physics, 88(9), 5272-5276.

[93] Yin, H., Cao, Y., Fan, T., Qiu, B., Zhang, M., Yao, J., ... & Chen, S. (2020). Construction of carbon bridged TiO2/CdS tandem Z-scheme heterojunctions toward efficient photocatalytic antibiotic degradation and Cr (VI) reduction. Journal of Alloys and Compounds, 824, 153915.

[94] Qasrawi, A., & Taleb, M. (2020). Enhancement of electrical performance of ZnSe thin films via Au nanosandwiching.

[95] Silva SRP, Amaratunga GAJ. Doping of rf plasma deposited diamond-like carbon films. Thin Solid Films. 1995;270(1–2):194-199.

[96] Alharbi, S. R., & Qasrawi, A. F. (2021). Effects of Au nanoslabs on the performance of CdO thin films designed for optoelectronic applications. Physica E: Low-dimensional Systems and Nanostructures, 125, 114386.

[97] Qasrawi, A. F., Irshaid, T. M., & Gasanly, N. M. (2021). Observation of in situ enhanced crystallization, negative resistance effect and photosensitivity in Tl2InGaSe4 crystals. Materials Science in Semiconductor Processing, 122, 105461.

الملخص

تشكيل وتشخيص طبقات AlSb/CdS المتغايره

في هذه الرسالة ، تم تحضير رقائق من إثميد الألومنيوم (AlSb) و كبريتيد الكادميوم (CdS) بتقنية التبخير الحراري على ركائز زجاجية وركائز ITO تحت ضغط تفريغ قدره 10^{-4} ملي بار. تم تشخيص الرقائق هيكليًا وبصريًا وكهربائيًا. ولوحظ أن رقائق AlSb و CdS تظهر طبيعة البلورات المكعبة والسداسية، على التوالي. وتم تحديد الخصائص الهيكلية بما في ذلك المعلومات الشبكية، وحجم البلورات، و microstrains، وكثافة الخلل وأخطاء التراص. أدى تبخير CdS على AlSb إلى زيادة كثافة الخلل وزيادة microstrains وتقليل أحجام البلورات. تُعزى التغييرات الهيكلية إلى عدم تطابق الشبكة وآليات الترابط بصريًا، أظهر كل من CdS و AlSb/CdS الانتقال المباشر خلال فجوة الطاقة البصرية 2.45 و 2.20 الكترون فولت، على التوالي. على الرغم من أنها ذات طابع معدني، فقد نجحت ركائز AlSb في تحسين امتصاص الضوء (R_λ) في النطاق المرئي للضوء الذي يظهر حدًا أقصى لِـ R_λ يبلغ 14.8 ضعف من مرات عند 2.21 فولت. أظهرت تحليلات أطياف العزل الكهربائي أن AlSb يمكن أن يُظهر قيمًا كبيرة لثبات العزل الكهربائي في نطاق الأشعة تحت الحمراء للضوء. انخفض ثابت العزل الكهربائي لِـ CdS بشكل ملحوظ عند التبخير على AlSb في نطاق الأشعة تحت الحمراء. من ناحية أخرى، سمح نموذج Drude–lorentz للجزء التخيلي من ثابت العازل الى تحديد تردد plasmon، وحركة الانجراف، وطاقة المذبذب ووقت الاسترخاء في مستوى الفيمتو الثانية. بينما أظهر AlSb أعلى تردد plasmon، أظهر CdS تحسن في ترددات plasmon. أدى تداخل الطبقتين إلى قيم معتدلة لحركة الانجراف وتردد plasmon. قيم تردد plasmon في نطاق جيجا هرتز تؤهل الرقائق المدروسة للاستخدام في تقنيات 4G/5G. كهربائياً، أظهر التحليل الطيفي للمانعة الذي تمت دراسته في النطاق الطيفي 10–1800 ميجاهرتز أن أجهزة (IAC) ITO/AlSb/C تظهر خصائص مرشح تمرير أعلى من 1800 ميجاهرتز و أجهزة (IACC) ITO/AlSb/CdS/C خصائص مرشح التوقف متعدد النطاقات فوق 1200 ميجاهرتز. أشار تحليل موصلية التيار المتردد إلى هيمنة توصيل بالقفز خلال أبار الطاقة المتجمعة (CBH) في تركيبه IAC والآلية المدمجة لِـ CBH والنفق الميكانيكي المكمم في أجهزة IACC. بينما تُظهر أطياف السعة لعينات IAC اتجاهًا متضخمًا مع زيادة التردد ، أظهرت عينات IACC ثلاث قمم رنين عند 217 ميجاهرتز و 829

ميجاهرتز و 1098 ميجاهرتز. لاستكشاف أصول طبيعة تكوين AlSb، كررت دراسة الخصائص التركيبية والكهربائية لبقايا مصدر التبخير AlSb. إحدى الميزات المثيرة للاهتمام هي أن طرف الجزء العلوي يتكون من 43٪ AlSb والقاع يتكون من 32٪. أظهرت هذه التركيبة لماده AlSb خصائص مرشح تمرير منخفض على تردد أعلى من 1600 ميجاهرتز. أظهرت الدراسة أنه يمكن استخدام الأغشية والعينات المتبقية بشكل فعال في التطبيقات الإلكترونية الضوئية.